SANDIA REPORT
SAND2014-17638
Unlimited Release
Printed August 2014

Modeling Macrosegregation in Directionally Solidified Aluminum Alloys under Gravitational and Microgravitational Conditions

Mark A. Lauer, David R. Poirier, Robert G. Erdmann, Surendra N. Tewari, Jonathan D. Madison

Prepared by
Sandia National Laboratories
Albuquerque, New Mexico 87185 and Livermore, California 94550

Sandia National Laboratories is a multi-program laboratory managed and operated by Sandia Corporation, a wholly owned subsidiary of Lockheed Martin Corporation, for the U.S. Department of Energy's National Nuclear Security Administration under contract DE-AC04-94AL85000.

Issued by Sandia National Laboratories, operated for the United States Department of Energy by Sandia Corporation.

Available to DOE and DOE contractors from
U.S. Department of Energy
Office of Scientific and Technical Information
P.O. Box 62
Oak Ridge, TN 37831

Telephone: (865) 576-8401
Facsimile: (865) 576-5728
E-Mail: reports@adonis.osti.gov
Online ordering: http://www.osti.gov/bridge

Available to the public from
U.S. Department of Commerce
National Technical Information Service
5285 Port Royal Rd.
Springfield, VA 22161

Telephone: (800) 553-6847
Facsimile: (703) 605-6900
E-Mail: orders@ntis.fedworld.gov
Online order: http://www.ntis.gov/help/ordermethods.asp?loc=7-4-0#online

SAND2014-17638
Unlimited Release
Printed August 2014

Modeling Macrosegregation in Directionally Solidified Aluminum Alloys Under Gravitational and Microgravitational Conditions

Mark A. Lauer, David R. Poirier, Robert G. Erdmann
The University of Arizona
Department of Materials Science & Engineering
P.O. Box 210012
Tucson, AZ 85721–0012

Surendra N. Tewari
Cleveland State University
Department of Chemical & Biomedical Engineering
2121 Euclid Ave., SH 455
Cleveland, OH 44115–2214

Jonathan D. Madison
Sandia National Laboratories
Org. 1814 Computational Materials & Data Science
P.O. Box 5800 MS-0889
Albuquerque, NM 87185–0889

Abstract

This report covers the modeling of seven directionally solidified samples, five under normal gravitational conditions and two in microgravity. A model is presented to predict macrosegregation during the melting phases of samples solidified under microgravitational conditions. The results of this model are compared against two samples processed in microgravity and good agreement is found. A second model is presented that captures thermosolutal convection during directional solidification. Results for this model are compared across several experiments and quantitative comparisons are made between the model and the experimentally obtained radial macrosegregation profiles with good agreement being found. Changes in cross section were present in some samples and micrographs of these are qualitatively compared with the results of the simulations. It is found that macrosegregation patterns can be affected by changing the mold material.

ACKNOWLEDGMENTS

The work herein is the result of collaboration with many people including: Samuel G. Angart, Luke Johnson, Masoud Ghods, and Dr. Richard N. Grugel. Funding for this work was provided by NASA Grants NNX08AN49G and NX10AV40G. The author/s also gratefully acknowledge support from the Sandia National Laboratories Campus Executive Graduate Research Program, which is funded by the Laboratory Directed Research and Development (LDRD) Program. Sandia is a multi-program laboratory managed and operated by Sandia Corporation, a wholly owned subsidiary of Lockheed Martin Corporation, for the US Department of Energy's National Nuclear Security Administration under Contract No. DE-AC04-94AL85000.

CONTENTS

FIGURES

TABLES

NOMENCLATURE

$\bar{C}$	Overall concentration of solute
C_l	Concentration of solute in the liquid
c_p	Specific heat capacity
C_{ref}	Reference (nominal) concentration of solute
C_s^*	Concentration of solute at the solid interface
$\bar{C}_s$	Average concentration of solute in the solid
d_A	Primary dendrite arm spacing
D_l	Diffusivity of solute in the liquid
f	Area fraction
G	Thermal gradient
$\boldsymbol{K}$	Darcy permeability tensor
k	Equilibrium partition ratio
L	Latent heat of fusion
l_g	Characteristic length scale
m_l	Slope of the phase diagram liquidus
p	Pressure
R	Radius of experimental sample
r	Radial cylindrical coordinate
S_{rms}	Macrosegregation Index
T	Temperature
t	Time
T_M	Melting point of pure material
T_{ref}	Reference temperature
$\boldsymbol{u}$	Superficial liquid velocity
V_0	Average solidification rate
V_{mig}	Migration velocity of a liquid droplet
W	Width of simulation domain
x	Horizontal Cartesian coordinate
z	Axial-cylindrical or one dimensional coordinate
$_{W,P,E}$	Node locations for discretization
$_{l,s,m}$	Liquid, solid, or mold property
$_{a,b}$	Value at present or future, t+dt, time
α	Thermal diffusivity
β_C	Coefficient of solutal expansion
β_T	Coefficient of thermal expansion
ν	Kinematic viscosity
ρ	Density
ρ^*	Boussinesq density
κ	Thermal conductivity
ϕ	Volume fraction liquid
∇	Differential operator

1. INTRODUCTION

This report covers a series of solidification experiments that were conducted to better understand the fundamental science of solidification. The particular aspects investigated in this report were that of macrosegregation of alloying elements that occurs during the directional processing and solidification of aluminum alloy samples. As part of this work, seven different experiments were run and samples created. The first two were Al-7wt%Si samples processed onboard the International Space Station under microgravity conditions. These samples were in straight sided cylindrical crucibles that that were melted and solidified in space as part of the MICAST research program. Three additional Al-7wt%Si samples were processed terrestrially, one in a straight sided crucible and two in shaped crucibles that had a central contraction to a smaller diameter cylinder and then an expansion back to the initial diameter. Additionally, two Al-19wt%Cu alloy samples that were processed terrestrially in identically shaped molds.

While analyzing the samples from these various experiments, it was found that macrosegregation of solute can occur during both the melting step of processing and the solidification period. However, it also quickly became apparent that it is difficult to treat both melting and solidification with a single model because of asymmetries between the two. In the microgravity experiments, macrosegregation during the melting period, turned out to be the predominant cause of macrosegregation and is examined first. The terrestrially samples also would have macrosegregation occurring during the melting phases, but convection would play a larger role, making it a much more challenging problem to model, so for the moment, this has been left unresolved. Modeling the solidification phase of the experiments has been the sole focus of the terrestrial modeling, which is likely the time period in which the majority of macrosegregation present occurred. The macrosegregation present was found in both straight sections of samples with constant diameter and at the changes in cross section. Each of these will be discussed in a section.

2. LITERATURE REVIEW

2.1 Macrosegregation During Melting

In recent years significant experimental attention has been given to the evolution of a mushy zone (intermixed solid and liquid phases) of an alloy melting or held in a thermal gradient [1-11]. In most of these experiments there are temperatures above the liquidus and below the eutectic leading to three distinct zones of all solid, mushy, and all liquid. Many studies have investigated the macrosegregation that develops in the mushy region because of solute-enriched liquid migration that is driven by solute diffusion. This liquid migration in the mixture of solid and liquid has been termed temperature gradient zone melting (TGZM) by Pfann [12]. A liquid in a liquid-solid mixture in a thermal gradient will likely have a spatially varying concentration of solute because of the thermodynamics of the solid-liquid equilibria at different temperatures. These concentration gradients lead to diffusion of solute through the liquid. The diffusion of solute results in melting on the hot side and solidification on the cold side of a liquid droplet, which in turn leads to migration of the droplet and overall solute macrosegregation.

Pfann suggested that the migration velocity of a liquid droplet in a temperature gradient could be given by:

$$\boldsymbol{V_{mig}} = \frac{-\boldsymbol{GD_l}}{\boldsymbol{m_l C_l (1-k)}} \qquad (1)$$

Nguyen Thi et al. [7,8] showed this to be the case using real time synchrotron radiography of drops of liquid in the mushy zone of an aluminum alloy. They also demonstrated that, as more solid forms, the thermal gradient decreases because of the higher thermal conductivity of the solid compared to the liquid. This causes the droplet velocity to decrease proportionally. Nguyen Thi et al. [7,8] presented a model to predict macrosegregation based on the droplet migration velocity. There is some difficulty in applying this migration velocity to liquid channels in the alloy and assumptions have to be made about the initial distribution of the droplets, which may make this model difficult to apply.

Gewecke and Schulze [13,14] introduced a model that captures most of the macroscopic phenomena observed during TGZM. This model covers the all-solid, mushy and all-liquid regions. In the all-liquid region they modeled the solute diffusion, but in the mushy zone rather than looking a migrating droplets they looked at the time evolution of the fraction liquid and showed that the tips of the mushy zone retreat and the all-solid region advances until they meet and a plane front is established. Salloum et al. [15] generated experimental data that provided qualitative confirmation of the calculations of Gewecke and Schulze. Fischer et al. [2] also got reasonable agreement with experimental results using a similar fraction-liquid evolution model, but they neglected diffusion in the all-liquid region. The model presented herein is similar to these two models, but unlike the model of Gewecke and Schultz[13,14], this model includes solute partitioning to the solid as well. Handling of solute partitioning at the eutectic interface is also treated differently. The evolution of the temperature field is

also included as well. This new model is compared with models based on the migration velocity of liquid droplets.

2.2 The Steepling Phenomena

The aluminum alloys studied in this research exhibit a stabilizing density gradient when solidified upwards in normal gravitational conditions because they partition a heavier solute into the liquid. However, it has been shown that under slow solidification rates any small horizontal density gradient can be destabilizing and lead to convection, by a mechanism known as "steepling." The steepling, sometimes called radial macrosegregation, phenomenon was first reported by Burden et al. [16] who presented results for solidifying several hypoeutectic Al-Cu alloys of different Cu concentrations vertically in cylindrical crucibles. Despite efforts to the contrary, solidification experiments have at least some small radial thermal-gradient in the region of solidification. This radial gradient begins the convection, and the flowing liquid advects solute along with it. The solute inhibits solidification where it is advected, and a strongly curved, or steepled, solidification front develops. The resulting structure in metallic alloys solidified directionally at slow rates is usually a solute depleted region of primary dendrites in the center of the sample and a solute enriched region of dendrites and/or eutectic constituent towards the outer edge.

Significant experimental works on steepling have been published. Burden et al. [16] and McCartney and Hunt [17] performed experiments in Al-Cu alloys. Mason et al. [18] and Verhoeven et al. [19] investigated steepling using several lead alloys. Nguyen et al. [20] and Billia et al. [21] published results showing steepling in Al-Ni and Al-Si alloys.

There have been a few simulation efforts as well. Weiss et al. [22] used CRYSVUN software to simulate the steepling phenomena in a SCN-H_2O alloy, but few details of the model are presented. Zhou et al. [23] used a model of Navier-Stokes equations in the all-liquid region and Darcy's law for flow in a porous media for the mushy zone. Additionally these equations were coupled to energy and solute conservation equations. They successfully reproduced convection that resulted in a deformation of the solidification front similar to that seen in experiments. Rienhart et al. [24] simulated the steepling-convection pattern in an equiaxed sample grown at slow solidification rates using a cellular automata-finite element model.

This work simulates steepling in two dimensions and compares the simulations to experiments with two different alloys, Al-7wt%Si and Al-19wt%Cu, at different solidification rates and thermal gradients. Comparisons to experimental results are made.

2.3 Modeling Directional Solidification in Shaped Castings

Simulation of directional solidification has been driven mainly by understanding defects in directionally solidified superalloy-turbine blades. Although the area has been active, there are not many published simulations that consider geometries with a changing cross section or consider heat transfer in the mold or crucible that contains the casting. This paper presents results showing the influences of mold properties and geometries on a solidifying alloy.

Some work has been done on modeling directional solidification in geometries with changing cross sections. Felicelli et al. [25-27] did some of the earliest explorations of directional solidification and changing cross sections. They simulated solidification of a nickel-base alloy in 2D geometries, but the boundary conditions used were simple compared with real castings. Heat transfer through a mold or core was not simulated.

The only previous works simulating directional solidification that considered the mold material, geometry, and thermosolutal convection are those by Xu et al.[28-30] and Bai et al. [31]. They investigated several different alloys in turbine blade-like castings and incorporated heat transfer through a mold. In the course of their investigations they mostly focused on other aspects, such as back diffusion models or the use of electro-magnetic fields for convection stabilization, and less on the effects of mold materials and geometries.

Elliott et al. [32,33] have shown experimentally, and through simulation, how the thermal processing conditions and heat flow in a mold with changing cross sections can change the shape of the solidification front in the solidifying casting during directional solidification. Freckles and crystallographic defects were analyzed; however no macrosegregation measurements, or simulations, were presented. Sellamuthu et al. [34] have experimentally shown that directionally solidified castings can show macrosegregation in the regions of a change in cross section. They used a Ni-based alloy and found good agreement with the macrosegregation equations of Nereo and Flemings [35] at the change in cross section.

3. MODELING MACROSEGREGATION DURING MELTING

3.1 Experimental Procedure and Analysis

In this research, two samples were processed in microgravity in a Bridgeman furnace onboard the International Space Station. In the MICAST-6 and MICAST-7 experiments the alloy samples were 8 mm by 24 cm Al-7 wt.% Si bars encased in an alumina crucible that had a wall thickness of 6 mm. The furnace had a hot zone and a cold zone separated by insulating baffles forming an adiabatic zone with nearly unidirectional thermal gradients. When the samples were first loaded, the furnace was moved to a withdrawn position. The heaters were then powered on and the furnace brought up to temperature, which caused the very end of the hot side of the sample to melt. The moving furnace was then ``plunged'' over the fixed sample, which was then further melted. After some period of melting when the furnace temperatures had stabilized, the temperature of the hot zone was increased to a set point and some additional melting occurred. The temperature field was then allowed to stabilize for a period of time, about two hours in the case of MICAST-6 and one hour in the case of MICAST-7. In this nearly constant thermal field, the samples had regions of all-solid, mushy, and all-liquid. After this holding period, the solidification experiment began and the furnace was withdrawn from the fixed sample at a predetermined rate. During the holding period, significant macrosegregation occurred in the mushy region of the sample, which can be seen in Figure 1. The left side was colder and the band of white was the approximate location of the eutectic isotherm during the furthest extent of melting. To the right of that is a portion of the mushy zone that was present during the holding period prior to solidification and to the left of the white band is the terrestrially solidified seed crystal. The amount of eutectic micro-constituents and Si increases with distance away from the location of the eutectic isotherm because of diffusion in the liquid and corresponding redistribution of solute between the interdendritic liquid and dendritic solid.

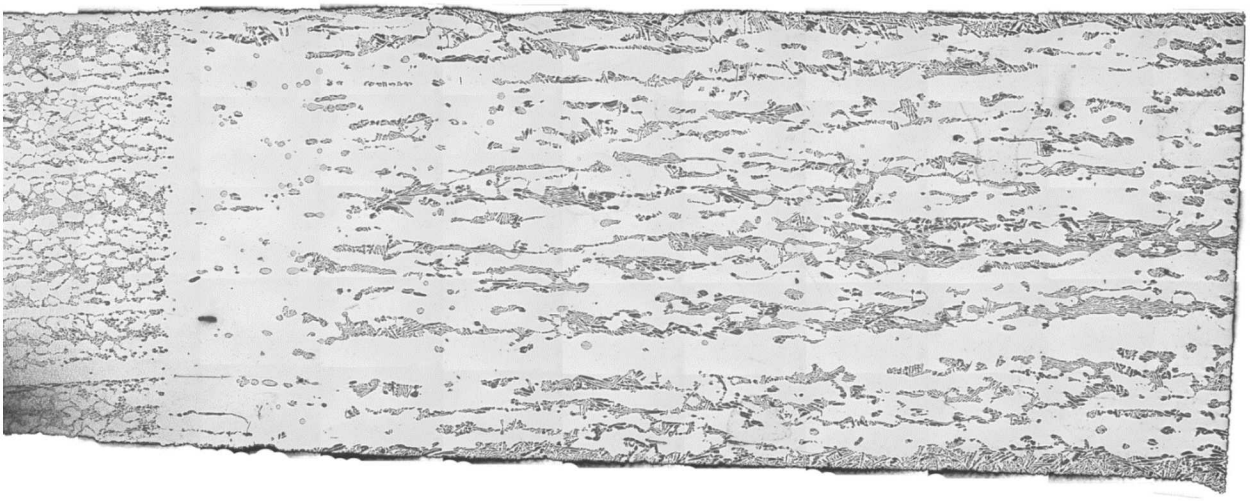

Figure 1. Thermal Gradient Zone Melting in MICAST-6.
Longitudinal section of the MICAST-6 sample showing the microstructure obtained after processing in microgravity.

Once the samples were returned to earth, specimens were taken and analyzed using Electron Microprobe Analysis (EMPA) on a CAMECA SX100 Ultra. The weight fraction of Si and Al was measured for each sample using the characteristic K_α X-ray. Pure Si and Al were used for calibration. Specimens taken from MICAST-6 and MICAST-7 were prepared using standard metallographic procedures to a high polish without any etching. The specimens were carbon coated and analyzed in an EMPA with a 31, 14, or 10 μm beam size to produce two-dimensional quantitative elemental X-rays maps. It was found that the 10 μm beams size gave the best results. The data from the other beam sizes are included in the plots to show that macrosegregation features were consistent across beam size. The MICAST-7 sample was ground approximately 1.5 mm between the first analysis using a beam size of 31 μm and the second using 10 μm, showing that the analysis is consistent across depth, and the one-dimensional assumptions in modeling are valid. The settings for EMPA 10 μm beam size analysis were an accelerating voltage of 10 keV, at 40 nA, and a dwell time of .01 s. Over the course of imaging, minimal drift was detected as current only shifted +/- 1 nA.

The EMPA two-dimensional X-ray maps were analyzed and found to be higher in concentration (~8 wt.%) of Si than the alloy was prepared at (7.0 wt.% Si). There is a difficulty with EMPA when analyzing the eutectic micro-constituent, because the beam overlaps two phases at the same time and the measured Si (present as needles in the eutectic micro constituent) is too high as a result. In the primary Al phase, the Si values were consistent with expected values, so the beam overlapping phases is believed to be the major source of this error. To compare the samples and simulations, the choice was made to normalize the measured concentrations using the unmelted seed crystal as a reference and adjusting all the data such that the seed crystal was 7 wt.% Si. The two dimensional maps were averaged across the transverse direction to produce one-dimensional data in the longitudinal direction for comparison with the 1D simulations. There was no significant macrosegregation found in any specimen in the transverse direction.

3.2 Mathematical Model

3.2.1 Solute Conservation Equation

An equation governing the conservation of solute is used in this work to model the transient diffusion of solute in the mushy and all-liquid regions of the alloy. In the model, transport by advection of solute is neglected. This is permissible since the experiments were conducted in microgravity, in which very little convection should be present. Shrinkage flows were neglected since these flows are proportional to the solidification rate, which was very low during the melting period. Diffusion in the solid phase is four to five orders of magnitude slower than in the liquid and so does not appreciably contribute to macrosegregation and is neglected. The conservation equation is:

$$\frac{\partial \bar{C}}{\partial t} = \nabla \cdot \boldsymbol{\phi}\, \mathbf{D_l} \nabla \boldsymbol{C_l} \quad (2)$$

Where

$$\bar{\boldsymbol{C}} = (\mathbf{1} - \boldsymbol{\phi})\bar{\boldsymbol{C}}_{\boldsymbol{s}} + \boldsymbol{\phi} \boldsymbol{C_l} \quad (3)$$

$\bar{C}$ is the overall concentration of solute in the two-(or one-)phase region. The averaged concentration of solute in the solid, $\bar{C}_s$, is given by

$$\bar{\boldsymbol{C}}_{\boldsymbol{s}} = \frac{\mathbf{1}}{\mathbf{1}-\boldsymbol{\phi}} \int_{\boldsymbol{\phi}}^{\mathbf{1}} \boldsymbol{k C_l d\phi} \quad (4)$$

In the mushy zone, where two phases coexist, the concentration of solute in the interdendritic liquid of the mushy zone is assumed to be in local thermodynamic equilibrium and is given by the phase diagram. In the simulations presented here, the Al-Si phase diagram is linearized and the concentration of solute in the interdendritic liquid is given by:

$$\boldsymbol{C_l} = \frac{\boldsymbol{T}-\boldsymbol{T_M}}{\boldsymbol{m_l}} \quad (5)$$

A diffusion coefficient, estimated by Poirier [36] that is a function of both temperature and concentration was used for our calculations. It is given below for completeness and convenience.

$$\boldsymbol{D_l} = \boldsymbol{D_0} \boldsymbol{e}^{(\boldsymbol{Q}/\boldsymbol{RT})} \quad (6)$$

$$\frac{\boldsymbol{Q}}{\boldsymbol{R}} = \mathbf{3328} - \mathbf{335.8} \boldsymbol{C_l} + \mathbf{19.34} \boldsymbol{C_l^2} \quad (7)$$

$$\boldsymbol{D_0} = \boldsymbol{e}^{(-15.494 - 0.3909 C_l + 0.027572 C_l^2)} \quad (8)$$

Where Q is the activation energy for diffusion J/mol and D_0 is the usual "pre-exponential" constant (m^2/s). To give the reader an idea of the magnitude of the diffusion coefficient, it ranges from 8.43×10^{-9} m^2/s at 850 K and 12.6 wt.% Si, the eutectic temperature and concentration, to 5.41×10^{-9} m^2/s at 893 K and 7.0 wt.% Si, the nominal liquidus and concentration of the alloy.

3.2.2 Energy Equation

During the experiments, the temperature of the system was measured by thermocouples. These thermocouples were attached to the outside of the crucible/mold and did not directly measuring the temperature of the alloy itself. The crucible was alumina and in order to obtain the temperature gradient in the alloy, a simplified steady state energy equation was used.

$$\mathbf{0} = \nabla \cdot \boldsymbol{\kappa} \nabla \boldsymbol{T} \quad (9)$$

The temperature data from the thermocouples was used as boundary condition data. The gradient inside the sample tended to be about 10 percent lower than what was measured by the thermocouples. If it was neglected, an incorrect length for the mushy zone would be obtained. The temperature data does change in time, but very slowly. The characteristic time for the alloy sample to reach thermal equilibrium is estimated to be around only two seconds (l_g^2/α). Because of this, and previous experiences modeling this solidification experiment, it is reasonable to expect the sample to be very near a steady-state temperature distribution at all times, especially since temperature adjustments in the experiment were made on time scales of several minutes. The maximum cooling rate during solidification was only 0.06 K/s.

When the temperature changed during the simulation, the new fraction liquid, ϕ, is found by the constraints of Equations (3-5). If the temperature was less than the eutectic temperature of the alloy, then the fraction liquid was set to zero. An additional assumption is that all solid with concentration above the equilibrium value of kC_l immediately decomposed to a mixture of solid with composition of kC_l and a liquid at C_l given by Equation (5). This is supported by the experimental findings of Fischer and Rettenmayr [37].

3.2.3 Numerical Methods and Discretization

The finite volume method was used to solve the governing equations. The solute conservation equation is consistent across all domains, of solid, liquid, and mushy zone, but the variable that is the degree of freedom changes in order to maintain a linear system. In the all-liquid region, the fraction liquid is fixed at one, and the degree of freedom is the concentration of solute in the liquid phase, which satisfies:

$$\frac{\partial C_l}{\partial t} = \nabla \boldsymbol{D_l} \cdot \nabla \boldsymbol{C_l} \qquad (10)$$

In the mushy zone the concentration of solute in the liquid is fixed by the local thermodynamic equilibrium assumption of the solid and liquid and is given by the phase diagram and Equation (5). This in turn makes the fraction liquid the degree of freedom in the mushy zone, which must be consistent with:

$$\boldsymbol{C_l} - \boldsymbol{C_s^*}\frac{\partial \boldsymbol{\phi}}{\partial \boldsymbol{t}} = \nabla \cdot \boldsymbol{\phi D_l} \nabla \boldsymbol{C_l} \qquad (11)$$

C_s^* is the concentration of Si in the solid at the interdendritic solid-liquid interface, which is being melted or formed. If it is being formed, it is given by the equilibrium partition ratio, $C_s^* = kC_l$, but a history of the concentration of the solid must be kept to return the proper amount of solute in the case of melting.

Unfortunately, this form of the conservation equation has the same numerical stability issues that have been well documented in Burgers' equation. This means that the usual approach of using central differences is unstable to any discontinuity in fraction liquid

and a one-sided differencing, or upwinding scheme, should be used instead. The simplest upwinding discretization is:

$$C_{l,P} - C^*_{s,P}\frac{\phi^b_P - \phi^a_P}{\Delta t}\Delta z A = -A\phi^b_W D_{l,w}\frac{C_{l,P} - C_{l,W}}{\Delta z} + A\phi^b_P D_{l,e}\frac{C_{l,E} - C_{l,P}}{\Delta z} \quad (12)$$

where superscript ^{b} implies the value at time $t + \Delta t$ and superscript ^{a} implies the value at time t. The subscripts: $_P$ implies the central volume; $_E$ implies the value in the volume to the east, or right, $_e$ implies a value at the east, or right, interface between the center volume and the volume signified by $_E$; $_W$ implies the value of the volume to the west, or left, and $_w$ implies a value at the west, or left, interface between the center volume and the volume signified by $_W$. Higher order upwinding methods can be used, but are problematic when there are very large discontinuities in the fraction liquid, such as when melting past a region that has been held at the eutectic temperature for a significant time period.

Equation (12) can be rearranged to the convenient form of:

$$-\phi^a_p = -\frac{\Delta t}{(C_{l,P} - C^*_{s,P})\Delta z^2} D_{l,w}(C_{l,P} - C_{l,W})\phi^b_W + \left[\frac{\Delta t}{(C_{l,P} - C^*_{s,P})\Delta z^2} D_{l,e}(C_{l,E} - C_{l,P}) - 1\right]\phi^b_P \quad (13)$$

The all-liquid region is discretized in a standard second order central difference fashion of

$$-C^a_{l,P} = \frac{\Delta t}{\Delta z^2} D_{l,w} C^b_{l,W} - \left(\frac{\Delta t}{\Delta z^2}(D_{l,w} + D_{l,e}) + 1\right) C^b_{l,P} + \frac{\Delta t}{\Delta z^2} D_{l,e} C^b_{l,E} \quad (14)$$

Care needs to be taken for the volumes on the interface between the mushy and liquid regions because of the changing degrees of freedom in the governing equation. For example, for the last mushy volume (dendrite tips) before the all-liquid region (mushy-mushy-liquid) the discretization becomes:

$$-\phi^a_p + \frac{\Delta t}{(C_{l,P} - C^*_{s,P})\Delta z^2} D_{l,e}(C_{l,P}) = -\frac{\Delta t}{(C_{l,P} - C^*_{s,P})\Delta z^2} D_{l,w}(C_{l,P} - C_{l,W})\phi^b_W - \phi^b_P + \left[\frac{\Delta t}{(C_{l,P} - C^*_{s,P})\Delta z^2} D_{l,e}\right] C^b_{l,E} \quad (15)$$

There were five other special cases involving the interface of all-liquid volumes neighboring mushy volumes that also had to be specially discretized, but these discretization will be omitted for brevity. The cases are: mushy-liquid-liquid, liquid-mushy-liquid, liquid-liquid-mushy, mushy-liquid-mushy, and liquid-mushy-mushy.

A second problem that can occur is that there may be a discontinuity in the thermal gradient in the alloy if the difference in thermal conductivities between the solid and liquid is relatively large. This in turn leads to a change in the gradient in concentration. For the simulations presented, it was necessary to use the limit of the concentration gradient approaching from the mushy zone towards the liquid as the concentration

gradient between the mushy volume nearest to the all-liquid region and the next nearest. If this was not done, then a small oscillation in the fraction liquid developed in the simulation in the second to last volume next to the mushy zone before the all-liquid region because of the change in the thermal gradient. If there was no, or a relatively small, change in the thermal gradient at this point, no special treatment was necessary.

With these discretizations it is easy to develop an asymmetric linear system of equations in the form of:

$$\boldsymbol{Ax} = \boldsymbol{b} \qquad (16)$$

which could be quickly solved for the unknowns. The thermal properties of the Al-7wt%Si alloy that were used in the simulations are given in Table 1.

Table 1. Materials Properties Used in Melting Simulations

Material Properties	Value	Units
Liquid Thermal Conductivity	76.7	W/(m K)
Solid Thermal Conductivity	185	W/(m K)
Alumina Mold Thermal Conductivity	11	W/(m K)
Linearized Melting Temp. of Pure Al	946.15	K
Eutectic Temperature	850.15	K
Nominal Liquidus Temperature	892.82	K
Liquidus Slope	-7.619	K/wt.%
Equilibrium Partition Ratio, k	0.131	

3.2.4 Comparison with Droplet Migration Model

Consider a small droplet of uniform cross section. Using this model to analyze the droplet we would say that the excess solute in the liquid (above equilibrium solid concentration) of a small volume, $\Delta V = \Delta z A$, containing this droplet would be

$$\boldsymbol{C_{l,xs} = \Delta z\, C_l(1-k)A\phi} \qquad (17)$$

where Δz is the length of the droplet in the direction of the thermal gradient and A is the cross sectional area. When all of this excess solute has diffused across the droplet and the droplet has moved out of the volume is when the total flow of solute is equal to the excess solute. The flow is the flux multiplied by the area, multiplied by the time. The droplet has left the volume when

$$\boldsymbol{\Delta z\, C_l(1-k)A\,\phi = j * \Delta t A = -\phi\, D \nabla C_l \Delta t A} \qquad (18)$$

Realizing the $\nabla C_l = G/m_l$ the above expression can be rewritten

$$\frac{\boldsymbol{\Delta z}}{\boldsymbol{\Delta t}} = \frac{\boldsymbol{-DG}}{\boldsymbol{C_l(1-k)m_l}} \qquad (19)$$

In the limit of infinitely small volumes we get Pfann's expression of the migration velocity of a liquid droplet in a solid [38].

$$V_{mig} = \frac{-DG}{C_l(1-k)m_l} \quad (20)$$

This shows that droplet migration is a special case of the more general fraction liquid model. It also suggests why vertical channels in the experiments of Nguyen Thi et al. [7,8] presented difficulties to applying the droplet migration model. In those, the fraction liquid is varying in space, which is an assumption we could not make to recover the droplet migration.

3.3 Simulation Mesh and Initial and Boundary Conditions

The temperature field was solved using the FiPy simulation package developed by NIST [39]. The computational domain was a two dimensional cylindrical mesh of the sample alloy and surrounding crucible. The locations of the thermocouples were on the edge of the domain, and the recorded thermal data provided boundary conditions. The computational mesh used was 0.32 m long with $\Delta z = .0001$ m and was 0.01 m wide in the radial direction with Δr of 0.0005 m. It was found during testing that higher resolution was needed in the z-direction than the r-direction particularly at the tips of the dendrites of the mushy zone. Different volumes of the mesh were assigned the appropriate materials. Thermal conductivity was assigned by the material and phase present: solid Al, liquid Al, mushy Al, or alumina crucible. The mushy zone used a parallel thermal conductivity model based on the volume fraction of the phase since the primary aluminum dendrites are generally aligned with the temperature gradient. The boundary conditions at *r*=.01 (the outside edge of the crucible) were a third-order smooth spline fit through the data points from each of the 13 thermocouples recording the experiment. For the boundaries at *z*=0 and *z*=0.32 there were no thermocouple recordings. This was handled by including 0.04 m of crucible on each end of the aluminum sample and then setting the boundary conditions at the ends to be no heat flux beyond this additional included crucible. Because of the very high aspect ratio of this sample, the results were hardly dependent upon the boundary conditions chosen on the *z*=0 and *z*=0.32, as long as the choice was reasonable. The boundary condition at *r*=0 is no flux due to symmetry.

For solving the conservation of solute equation, Equation (2), custom software was written using the finite volume method for a one dimensional mesh of the alloy sample using the same spacing as the temperature mesh in the *z*-direction, but covering only the partially melted and all-liquid portions of the sample. The temperature simulations do show a relatively small radial component to the temperature gradients, and appreciable radial macrosegregation was not found in the samples. Consequentially, only a one-dimensional model was implemented. For the initial condition the sample was completely solid with no initial macrosegregation prior to melting. A Scheil solidification profile was assumed initially for a microsegregation model to determine the

concentrations of the solid, $\bar{C}_s$ and C_s^* and the fraction liquid, ϕ. Boundary conditions were no solute flux out of the crucible and no solute flux into the all solid region, corresponding to the assumptions of no solute diffusion in the solid.

The method of coupling of the governing equations is first solve the energy equation, Equation (9), for the temperature distribution and this temperature distribution is used to calculate the concentration of the liquid at every point in the mushy zone using Equation (5). The fraction liquid is then calculated from the solidification history and the constraints of conservation of solute in a volume and the phase diagram, Equations (3) and (4). At this point a diffusion time step was taken and the new distribution of ϕ in the mushy zone was determined simultaneously with the liquid concentration in the all-liquid region. The new values of ϕ were then used to calculate the thermal conductivity of the sample taking account that it is different between the solid and liquid, and the energy equation was solved once again. The process was repeated using the temperatures recorded by the thermocouples at the new time as boundary conditions. The time step used was two seconds, which was selected through iterative testing.

Coarser meshes with Δz-spacings of two to four times greater and larger time steps were run to verify the consistency of the results, which showed no differences beyond the expected loss of resolution.

3.4 Results and Discussion

Shown in Figure 2 are time points from the simulations to explain the final observed profile. The first panel of Figure 2(a) shows the state of the simulation at 6460 seconds into the experiment during the phase where the furnace is ``plunged'' over the sample and the sample rapidly melts. As can be seen from the curve labeled $\bar{C}$, which denotes the overall concentration, very little macrosegregation occurs during this rapid melting phase. The dashed lines labeled T_E and T_C are the non-dimensionalized temperature profiles for the outer edge of the crucible and the center of the sample respectively. The center temperature is the profile used in the 1D simulation to calculate macrosegregation. These non-dimensional values are read off the right hand scale, but are mainly displayed to show how furnace caused melting and solidification between frames. In the region of the mushy zone, the edge temperature profile is anywhere from about +5 K to -1 K hotter than the middle temperature in these simulations. The liquidus and eutectic temperatures for the alloy are shown by the dashed lines, highlighting the area of the mushy zone. The fraction liquid curve, labeled ϕ, shows the amount of liquid alloy that is involved in diffusive transport. The fraction liquid is read off the right hand scale. The discontinuity in the ϕ curve where it jumps from 0 to approximately 0.5 is the location of the eutectic isotherm and the location where is reaches 1 is the tips of the dendrites of the mushy zone and the mushy-all-liquid interface. At 6460 s is the shape predicted by a Scheil solidification profile since no macrosegregation has yet occurred. The C_l curve, which is read off the left hand scale, shows the concentration of Si in the liquid phase and the steep gradient of that curve in the mushy zone is the

driving force for the diffusive transport. It joins the $\bar{C}$ curve is the all-liquid region, since these concentrations are identical in value there.

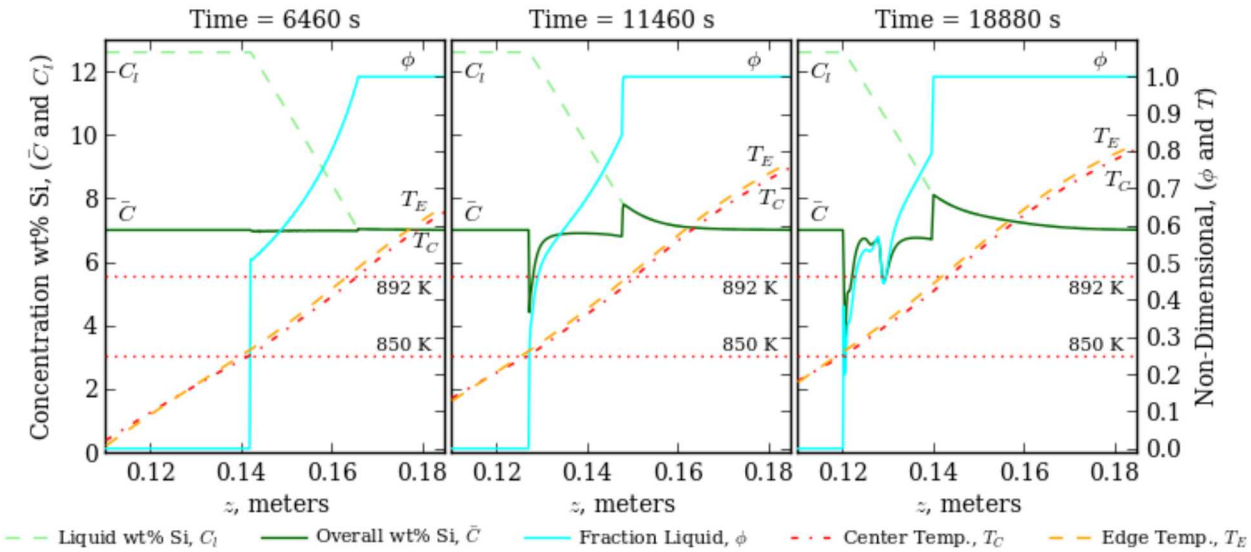

(a)

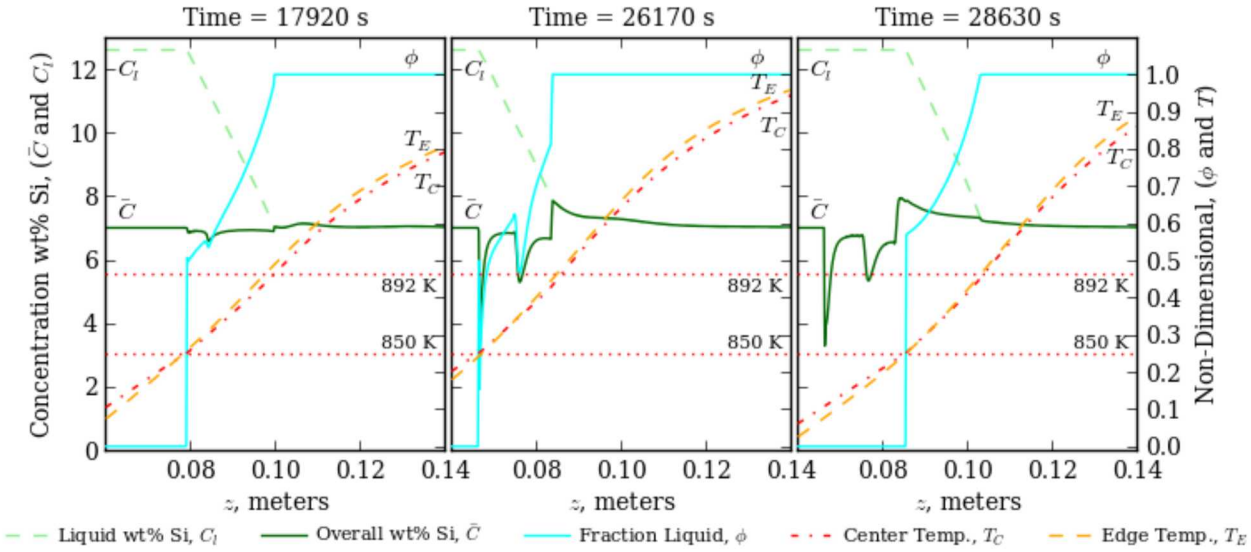

(b)

Figure 2. Time Series Showing Simulation States.

Plots of simulation states at different points in time. The concentration lines are read by the scale on the left. The temperatures are non-dimensionalized, $(\mathrm{T} - 800\ \mathrm{K})/\ (1000\ \mathrm{K} - 800\ \mathrm{K})$, and read off the right hand scale with the nominal temperatures corresponding to the mushy zone shown by the dotted lines. The fraction liquid is read off the right hand scale as well. (a) MICAST-6 showing a time during melting back at 6460 s into the experiment, then after a period of holding at 11460 s, and finally after further melting back and holding at 18880 s. (b)MICAST-7 during the early melt back stage, but before holding at 17920 s, after further melting and holding at 26170 s, and during the solidification phase of the experiment at 28630 s.

In the second panel of Figure 2(a) the temperature profile has been held for some period during the melt-back, and negative macrosegregation begins to develop at the location of the eutectic isotherm as can be seen by the sharp dip in the $\bar{C}$ curve. This macrosegregation rapidly occurs at the eutectic isotherm because solute is diffusing out of the mushy zone, but no solute diffuses in from the solid phase. It can also be seen in the $\bar{C}$ curve that positive macrosegregation begins to develop at the tips of the dendrites as solute that is diffusing out of the mushy zone builds up a boundary layer in the all-liquid region. The tips of dendrites begin to melt back and the length of the mushy zone decreases, which can be seen in the blunting of the shape of the ϕ curve at the mushy-all-liquid interface. If the melting back is continued from this point, as seen in the third panel of Figure 2(a), there will be a region in the mushy zone corresponding to the former eutectic isotherm that has extreme negative macrosegregation, which is seen the graphs as the second dip in the $\bar{C}$ curve and the corresponding dip in the ϕ curve.

The progression of the MICAST-7 simulation is shown in Figure 2(b). It proceeds in a similar manner as MICAST-6 describe above. Additionally shown in the third panel of Figure 2(b), is that when solidification proceeds, the significant boundary layer of solute in front of the mushy zone becomes enveloped by the advancing dendrite and become a region of positive macrosegregation in the solidified samples.

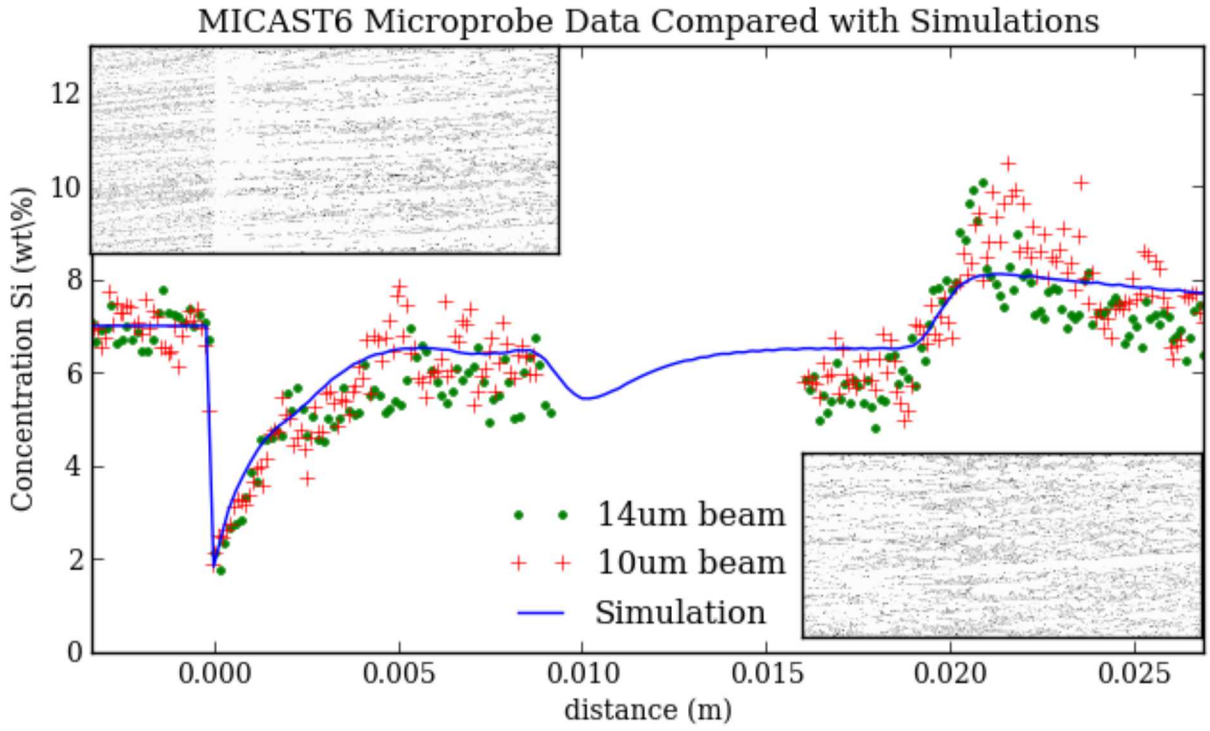

Figure 3. MICAST-6 Simulation and EMPA Concentrations.

MICAST-6 sample showing the silicon content of the region of mushy zone that was held for about 130 minutes in a temperature gradient at the maximum extent of melting. The inset figures are the EMPA x-ray maps with the microstructure and macrosegregation clearly visible.

Macrosegregation in the samples is shown in Figure 3 and Figure 4 as are the final macrosegregation profiles from the simulations. The simulations predict the shape of the macrosegregation and the length of the mushy zone present during the holding period. The process is diffusion controlled, so some of the difference between the measured and simulated results could be attributed to the uncertainty in the diffusion coefficient of Si in liquid Al. Poirier [36] states that very little experimental data are available for the diffusivity of Si in liquid Al, the available diffusivities presented are from molecular dynamics simulations. Another explanation is that a form of transport is not accounted for in the model. The two most likely are thought to be advection from shrinkage flows, which during melting would push high solute interdendritic liquid out of the mushy zone causing melting and widening of channels, and during the solidification would "pull" liquid of lower solute concentration into the mushy zone leading to some negative macrosegregation as describe by Flemings and Nereo [35]. Another possible form of transport is thermo-migration/Soret diffusion, but no data were found to be available for the Al-Si system and some of the fundamental issues surrounding it do not seem well understood. Another possibility relates to the earlier mentioned difficulties of measuring concentrations of a two phase region using an electron beam microprobe.

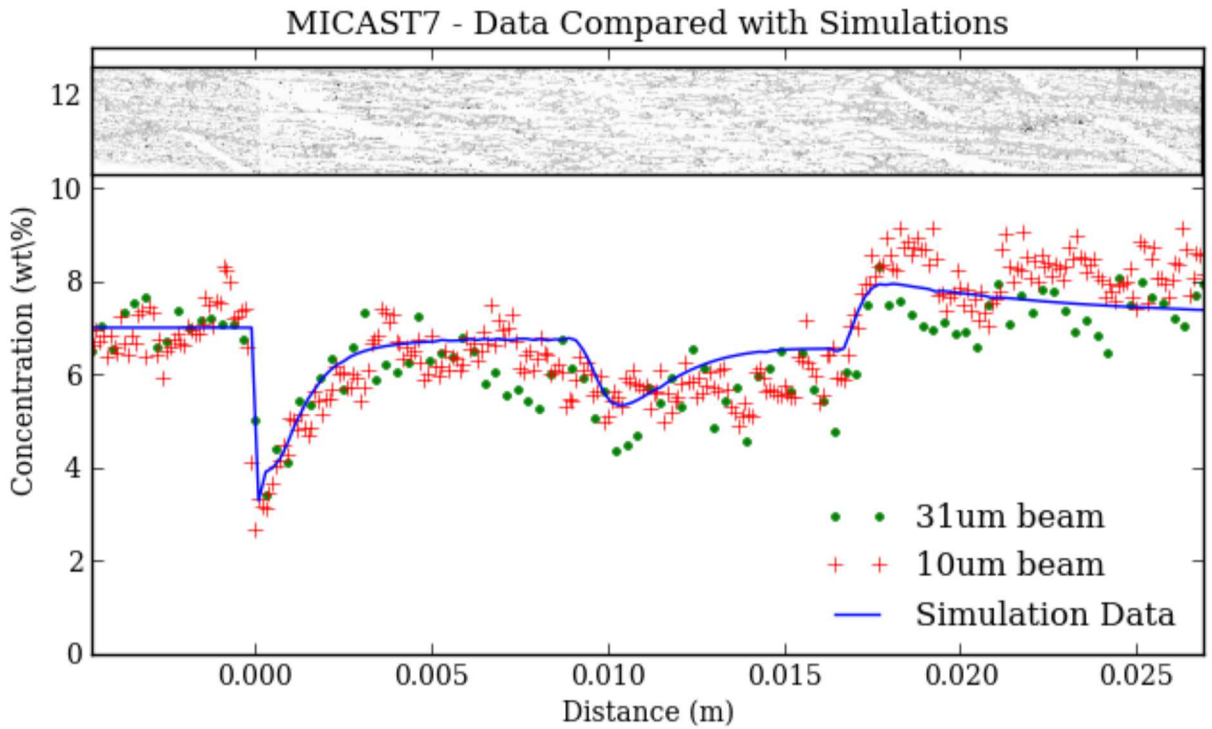

Figure 4. MICAST-7 Simulation and EMPA Concentrations.
MICAST-7 sample showing the silicon content of the region of mushy zone that was held for about 45 minutes in a temperature gradient at the maximum extent of melting. The inset figure is the EMPA x-ray map.

As can be seen in Figure 3 and Figure 4, there is significant noise in the measured EPMA data. Some of the larger scale noise comes from ``ghost'' dendrites that can be seen in the right inset of Figure 4 particularly in the all-liquid region during the holding period. Different levels of grinding also would lead to slightly different segregation profiles. This was checked in MICAST-7 and results are plotted in Figure 4.

In the MICAST-6 sample, the simulations under predict the solute concentration at the tip of the mushy zone. The reason for this is unknown, but may relate to a transient phenomenon in the initial solidification stage that is not captured by this simplified model. The model does correctly predict the depleted region seen in Figure 4 where the eutectic isotherm was rather stationary for a period of time during the melt-back. Unfortunately in MICAST-6, a sectioning cut was made in this area for purposes of characterizing the microstructure prior to knowledge of this negative macrosegregation, which results in the missing data in Figure 3. In both cases, the model makes excellent predictions of the negative macrosegregation at and near the eutectic isotherm location during the holding period.

4. MODELING DIRECTIONAL SOLIDIFICATION WITH CONVECTION

Modeling solidification in microgravity is possible without considering convection and flow, but quick becomes erroneous when applied to solidification problems under normal circumstances. To this end, an existing solidification code was modified and extended to analyze both solidification in microgravity and under normal gravitational conditions. This code however was not extended to cover melting due to complexity, so the previously introduced model was used for modeling that period and then the solution ported over as an initial condition for the new model, which is summarized below. For more information and to see previous work involving this model, see Felicelli, et al. [26,40,41].

This model was then used to analyze the two previous microgravity experiments and five terrestrial experiments conducted under the direction of Prof. Surendra N. Tewari at Cleveland State University. In these experiments, an Al-7wt%Si or Al-19wt%Cu alloy was solidified directionally upwards in a cylindrical graphite mold with a change in cross section from a 9.5 mm diameter region to a narrower 3.2 mm diameter region and then through an expansion back to 9.5 mm. The outer diameter of the graphite mold was 27.9 mm. The sample was melted back to a seed crystal in a Bridgeman furnace and then withdrawn vertically at 10, or 29.1 μm/s. Four thermocouples were placed along the outer part of the mold, and temperatures at these thermocouples were recorded throughout the entire experiment. The locations of these thermocouples are shown in Figure 5. A fifth sample of Al-7wt%Si that was in a straight sided crucible of 8mm inner diameter was also run at a solidification rate of 72 μm/s. This section analyzes the straight sections of the castings and the steepling that occurs there while the next section will cover the changes in cross section.

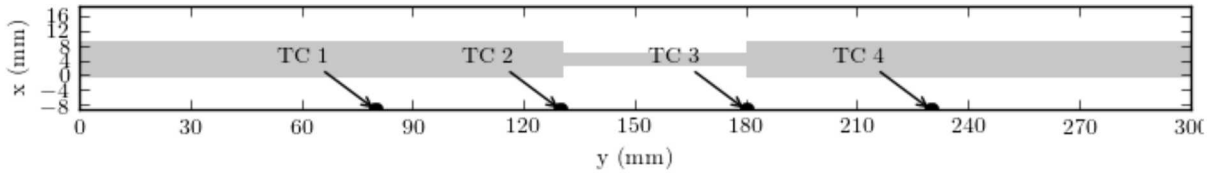

Figure 5. Mesh Geometry and Thermocouple Location.
Domain of changing cross section mold used in investigations. Grey shows alloy region, white shows mold. Thermocouple number and location are shown by the "TC #" labels.

4.1 Mathematical Model

The governing equations of the alloy solidification model used, which includes thermosolutal convection, were derived by Poirier et al. [42] and Ganesan and Poirier [43]. The governing equations are a volume averaged treatment of the solid, mushy, and liquid regions so that the entire solidifying alloy can be treated as a single domain. The numerical implementation is covered in detail by Felicelli et al. [26,40,41] and McBride et al. [44], and each of the governing equations are briefly discussed here.

4.1.1 Continuity Equation

Shrinkage flow from the difference in density between the solid and liquid phases is included in the continuity equation, which is:

$$(\boldsymbol{\rho_l} - \boldsymbol{\rho_s})\frac{\partial \boldsymbol{\phi}}{\partial \boldsymbol{t}} + \boldsymbol{\rho_l \nabla \cdot u} = \boldsymbol{0} \qquad (21)$$

Shrinkage induced flows can reduce the tendency for the thermosolutal convection cells to develop and is one of the reasons for the disappearance of steepling effects at increasing solidification rates. The strength of the shrinkage flow is directly proportional to the solidification rate and tends to reduce the steepling convection.

4.1.2 Momentum Equation

The momentum equation used in the model seamlessly transitions from Darcy's law, governing flow in a porous media in the low permeability mushy zone, to the Navier-Stokes equations in the all-liquid region.

$$\frac{\partial \boldsymbol{u}}{\partial \boldsymbol{t}} + \frac{\boldsymbol{u}}{\boldsymbol{\phi}} \cdot \boldsymbol{\nabla u} - \frac{\boldsymbol{\rho_s - \rho_l}}{\boldsymbol{\rho_l \phi}}\frac{\partial \boldsymbol{\phi}}{\partial \boldsymbol{t}}\boldsymbol{u} = -\frac{\boldsymbol{\phi}}{\boldsymbol{\rho_l}}\boldsymbol{\nabla p} + \frac{\boldsymbol{\rho^* \phi}}{\boldsymbol{\rho_l}}\boldsymbol{g} + \boldsymbol{\nu}[\boldsymbol{\nabla^2 u} - \boldsymbol{\phi K^{-1}} \cdot \boldsymbol{u} + \frac{\boldsymbol{\rho_s - \rho_l}}{\boldsymbol{3\rho_l}}\boldsymbol{\nabla}\frac{\partial \boldsymbol{\phi}}{\partial \boldsymbol{t}}] \qquad (22)$$

The Boussinesq approximation of the liquid density is assumed:

$$\boldsymbol{\rho^*} = \boldsymbol{\rho_l}[\boldsymbol{1} + \boldsymbol{\beta_T}(\boldsymbol{T} - \boldsymbol{T_{ref}}) + \boldsymbol{\beta_C}(\boldsymbol{C_l} - \boldsymbol{C_{ref}})] \qquad (23)$$

ρ^* accounts for the thermal and solutal effects on density that are necessary to capture thermosolutal convection because of buoyancy forces arising from variations in temperature and solute concentration in the liquid.

4.1.3 Solute Conservation Equation

$$\frac{1}{\boldsymbol{\rho_l}}\frac{\partial \overline{\boldsymbol{\rho C}}}{\partial \boldsymbol{t}} + \boldsymbol{u} \cdot \boldsymbol{\nabla C_L} = -\frac{\boldsymbol{\rho_s - \rho_l}}{\boldsymbol{\rho_l}}\mathbf{C_l}\frac{\partial \boldsymbol{\phi}}{\partial \mathbf{t}} + \boldsymbol{\nabla} \cdot (\boldsymbol{\rho_L D_e \nabla C_L}) \qquad (24)$$

Where

$$\overline{\boldsymbol{\rho C}} = \boldsymbol{\rho_s}\,(\boldsymbol{1} - \boldsymbol{\phi})\overline{\boldsymbol{C}}_\mathbf{s} + \boldsymbol{\rho_l}\,\boldsymbol{\phi}\,\mathbf{C_l} \qquad (25)$$

and

$$\overline{\boldsymbol{C}}_\boldsymbol{s} = \frac{\boldsymbol{1}}{\boldsymbol{1-\phi}}\int_{\boldsymbol{\phi}}^{\boldsymbol{1}} \boldsymbol{kC_l d\phi} \qquad (26)$$

The concentration of solute in the interdendritic liquid of the mushy zone is assumed to be in local thermodynamic equilibrium and given by the phase diagram. In the simulations presented here, the phase diagrams are linearized and the concentration of solute in the interdendritic liquid is given by:

$$\mathbf{C_l} = \frac{T - T_m}{m_l} \quad (27)$$

4.1.4 Energy Equation

$$\overline{\rho c_p}\frac{\partial T}{\partial t} + \rho_s\left[(c_{ps} - c_{pl})(T_{ref} - T) + L\right]\frac{\partial \phi}{\partial t} + \rho_l c_{pl}\boldsymbol{u}\cdot\nabla T = \nabla\cdot\kappa\nabla T \quad (28)$$

Where

$$\overline{\rho c_p} = \rho_s\,(1-\phi)c_{ps} + \rho_l\,\phi c_{pl} \quad (29)$$

In the mold or crucible material only the energy equation is applied, and simplifies to:

$$\rho_m c_{pm}\frac{\partial T}{\partial t} = \nabla\cdot\kappa_m\nabla T \quad (30)$$

The approximation of complete mold-alloy thermal contact is assumed, and no heat transfer coefficients are applied at the alloy-mold interface.

4.1.5 Fraction Liquid

In calculating the fraction liquid, Scheil-like assumptions are used. Within the mushy zone, the concentration of the liquid is given by Equation (27), and a history of the concentration of the solid is kept using Equation (26). The fraction liquid is found from the constraints of Equation (27) and Equation (25). This scheme allows for accurate remelting of the solid if warranted. For the multi-component version and more details see Felicelli et al. [25]. The finite element formulation is used to solve all of the governing equations in an iterative manner. Iterations stop when fraction liquid has converged to within a suitable tolerance for the time step. %All of the advection terms are treated explicitly using a Petrov-Galerkin upwinding scheme to prevent over-diffusion due to advection.

4.1.6 Permeability Model

The permeability model used was first used by McBride et al. [44] and later by Frueh et al. [45]. Since the experimental samples had columnar-dendritic or single-crystal dendritic microstructures, the permeability used is a tensor with one component perpendicular, K_x, and one parallel, K_y, to the direction of solidification.

$$K = \begin{bmatrix} K_x & 0 \\ 0 & K_y \end{bmatrix} \quad (31)$$

$$\begin{aligned} K_x &= 1.09\times10^{-3}\mathrm{d}_A^2\phi^{3.32},\ \phi < 0.65 \\ &= 4.04\times10^{-6}\mathrm{d}_A^2\left(\frac{\phi}{1-\phi}\right)^{6.7336},\ 0.65 \le \phi \le 0.75 \\ &= \left(-6.49\times10^{-2} + 5.43\times10^{2}\left(\frac{\phi}{1-\phi}\right)^{\{0.25\}}\right)\mathrm{d}_A^2,\ 0.75 \le \phi \end{aligned} \quad (32)$$

$$K_y = 3.75\times10^{-4}\phi^2,\ \phi < 0.65$$
$$= 2.05\times10^{-7}d_A^2\left(\frac{\phi}{1-\phi}\right)^{10.74},\ 0.65 \le \phi \le 0.75$$
$$= 7.42\times10^{-2}d_A^2\left(-\log(1-\phi) - 1.49 + 2(1-\phi) - \frac{(1-\phi)^2}{2}\right),\ 0.75 \le \phi \quad (33)$$

This permeability model assumes that the main trunks of the dendrites are oriented parallel to the direction of growth. The permeability in the region of the dendrite tips is a key parameter of the simulations, because much of the transport of solute-rich liquid occurs in this region.

4.2 Experimental Data

Three Al-7wt%Si and two Al-19wt%Cu samples were solidified in a Bridgman furnace. The Al-7wt%Si samples were solidified at pull rates of 10, 29.1, and 72 μm/s, while the Al-19wt%Cu samples were solidified at 10 and 29.1 μm/s. The crucible that contained the samples was graphite with an inner diameter of 9 or 9.5 mm and an outer diameter of 18.4 or 19 mm. It should be noted that several of these samples were solidified in the crucible with a constriction in cross section down to 3.2 mm in the center as part of a larger investigation. This central constriction does have some effect on the fluid flow and heat transfer through the mold and alloy when compared to a straight-sided crucible. The effect decreases after a few mushy zone lengths away from the constriction, and phenomena simulated here would also be observed in a straight-sided crucible.

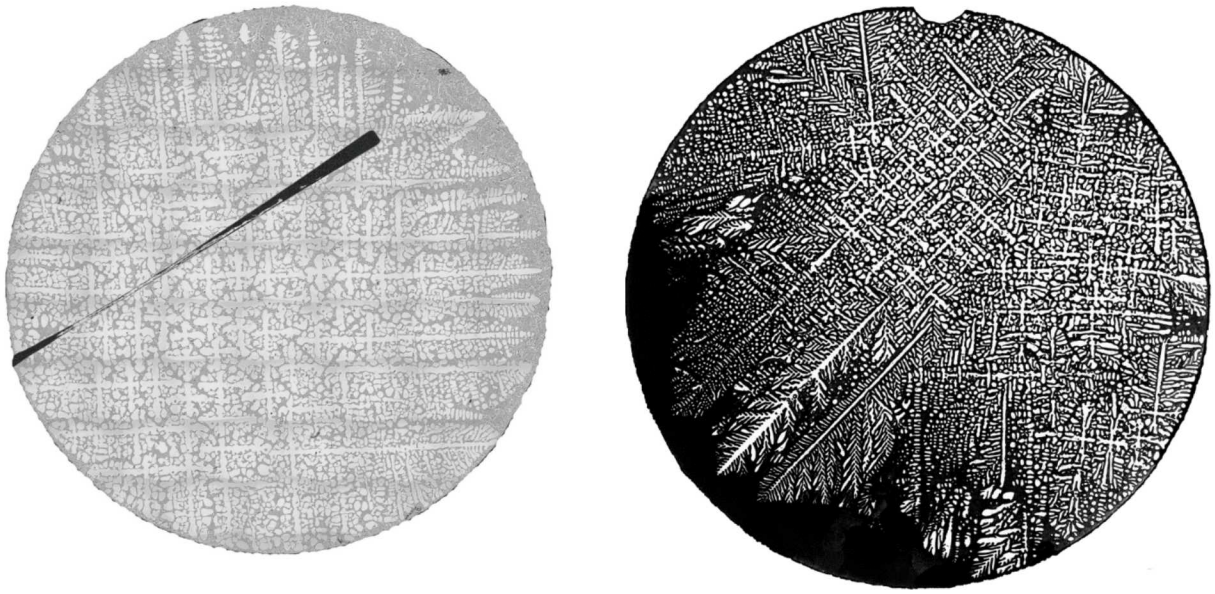

(a) (b)

Figure 6. Composite transverse micrographs

(a) Al-7wt\%Si solidified at 10 μm/s. (b) Al-19wt\%Cu solidified at 10 μm/s.

Composite micrographs from various locations, such as those seen in Figure 6, were made and the macrosegregation was measured using an image processing technique to extract fraction eutectic and related that to composition. Details pertaining to solidification and to measuring segregation are contained in Johnson et al. [46]. Note in that work the nominal concentration was not always 7wt%Si or 19wt%Cu. The choice was made to normalize the data to these values and then compare to the simulations contained herein.

4.3 Simulations

4.3.1 Mesh, Initial, and Boundary Conditions

In the simulations presented here, the appropriate geometry was meshed in two dimensions using Cartesian quadrilateral elements. The mesh was constructed to be refined near the edges of the crucible to better capture the convection occurring there and to reduce a numerical artifact of not being able to advect solute to the wall where there is no liquid velocity [40]. The mesh was constructed so that the largest elements were approximately half the primary dendrite arm spacing, which was found to be a useful criterion by Frueh et al.[45,47]. The constriction in cross section was included in the mesh when it was present. All experiments with the same geometries used the same mesh. Material properties for both alloys and the graphite mold are presented in Table 2.

The initial conditions for all simulations were that the alloy in the crucible was all liquid with no initial macrosegregation. In the simulations, the alloy was then rapidly cooled to the initial temperature profile from the experiments. This gave a condition close to the initial melting back of the solid-sample in the experiments. At this point, the temperature profile recorded by thermocouples placed along the sample during the withdrawal period was applied to the outer perimeter of the crucible as a function of time until the sample solidified completely. Other boundary conditions for the simulations were no slip and no penetration by the liquid on the melt-crucible interfaces. A small portion of the boundary at the top of the simulation domain was left open to accommodate flow to satisfy the continuity equation because of solidification shrinkage. No solute diffusion was allowed into the crucible. The temperature was set to a cooling profile on the entire outer perimeter for each time step based on thermocouple data gathered during the experiment.

Table 2. Material Properties Used for Convection Simulations

Alloy Properties [48-57]	**Al-7wt%Si**	**Al-19wt%Cu**	**Units**
Liquid Thermal Conductivity	76.7	77	W/(m K)
Liquid Heat Capacity	1070	972	J/(kg K)
Liquid Density	2408	2792	kg/m^3
Liquid Thermal Diffusivity	2.98×10^{-5}	2.84×10^{-5}	m^2/s
Solid Thermal Conductivity	185	152	W/(m K)
Solid Heat Capacity	1171	1066	J/(kg K)
Solid Density	2545	3006	kg/m^3
Solid Thermal Diffusivity	6.21×10^{-5}	4.74×10^{-5}	m^2/s
Viscosity	1.16×10^{-3}	1.65×10^{-3}	$N\ s/m^2$
Volumetric Expansivity of Liquid	-1.85×10^{-4}	-1.85×10^{-4}	K^{-1}
Solutal Expansion Coefficient	1.31×10^{-3}	2.35×10^{-2}	$wt.\%^{-1}$
Solute Diffusivity in the Liquid	4.2×10^{-9}	3.5×10^{-9}	m^2/s
Latent Heat of Fusion	5.31×10^{5}	3.71×10^{5}	J/k
Partition Ratio	0.131	0.170	
Linearized Melting Temp. of Pure Al	946.15	936.94	K
Eutectic Temp.	850.15	821.15	K
Nominal Liquidus Temperature	892.82	870.28	K
Liquidus Slope	-7.619	& -3.508	K/wt.%
Mold Properties	**Graphite**	**Alumina**	**Units**
Thermal Conductivity	65	11	W/(m K)
Heat Capacity	1570	1100	J/(kg K)
Density	2100	3900	kg/m^3
Thermal Diffusivity	1.97×10^{-5}	2.56×10^{-6}	m^2/s

4.3.2 Interpolating and Extrapolating Thermocouple Data

In the experiments, between one and four thermocouples were placed in circumferential grooves machined in the graphite crucible in order to record the thermal history during the experiment. The closest of these thermocouples were 5 cm apart. Since the boundary conditions require that the temperature be given for each boundary node at every time step during the simulation, the limited data had to be interpolated and extrapolated for all times and locations. Data points on the hot and cold ends of the sample were generated using the temperature of the nearest thermocouple data shifted in time by the distance to the end divided by the withdrawal speed. The best method was found to be fitting the data from the four thermocouples and data generated at the ends with a third-order interpolating spline of equal weights. If there was only one thermocouple on the sample, the time points were multiplied by the withdrawal rate to generate a temperature versus distance profile. In the simulations this thermal profile was translated across the sample at the withdrawal rate of the experiment.

It was found that the method of interpolating the thermocouple data did have an effect on the quantitative results obtained, but qualitatively the simulations revealed the same results. The thermocouple spacing of 5 cm represents around four to five mushy zone

lengths. In hindsight, increasing the number of thermocouples would have improved the spatial resolution of the data and improved the simulations.

4.4 Results

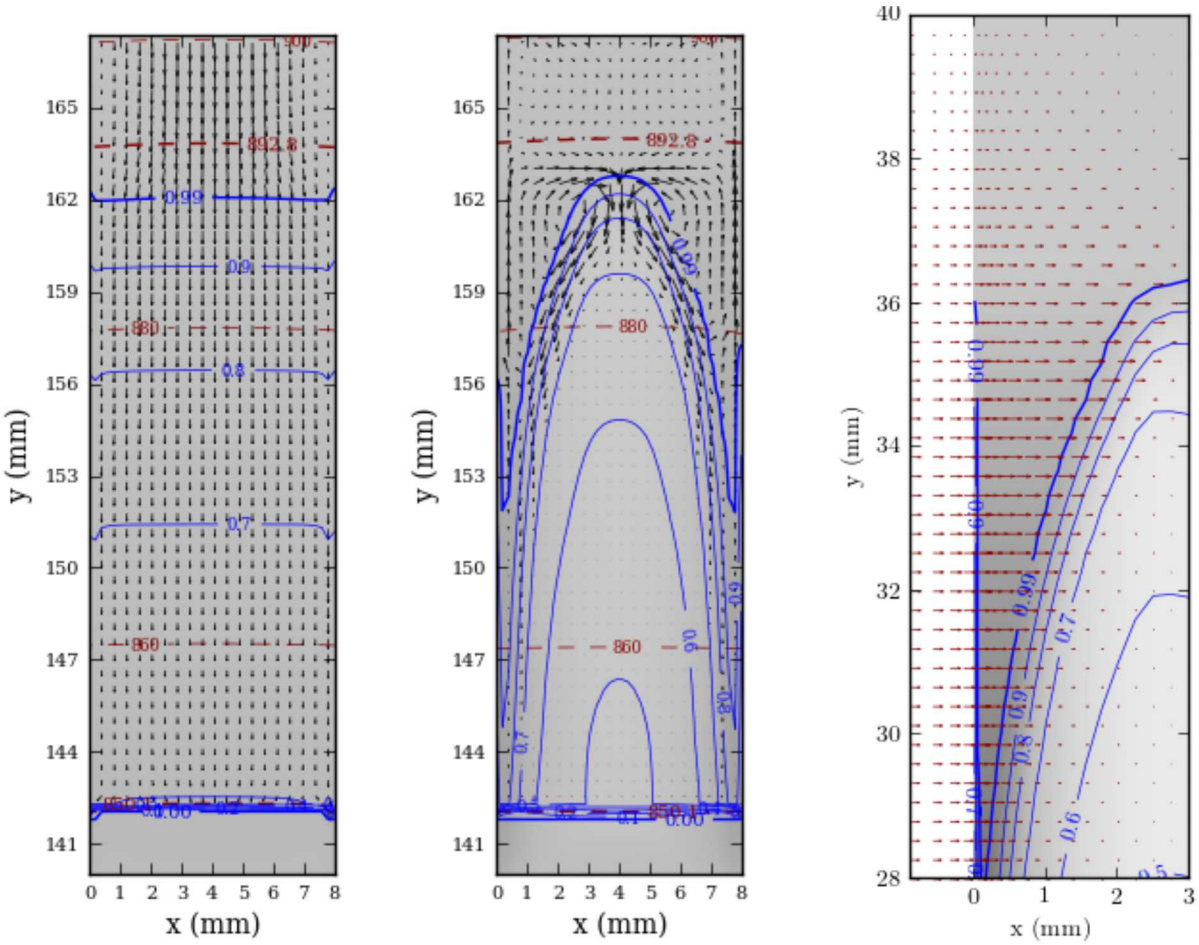

Figure 7. Micro-gravity vs. Normal Gravity.
Results from the MICAST-6 simulations, only a subsection of the domain is shown. Shading indicates solute concentration. Blue lines indicate isopleths of fraction liquid. Dashed red lines show isotherms. (a) Simulations of solidification in microgravity at 5 µm/s. (b) Simulation of solidification in normal gravity at 5 µm/s. (c) Detail view showing only the horizontal component of the heat flux to demonstrate the flow of heat from the mold to the alloy in the area of the solidification front causing the rounded steepling front under normal gravitations conditions.

The convection in the region of the solidifying dendrite tips for the microgravity and terrestrial experiments is strikingly different, as shown in Figure 7. The microgravity simulation, in Figure 7(a), shows well organized parallel flow that goes from parabolic in the all liquid region to plug like flow after it enters the mushy zone. For the normal

gravity experiment there are thermal convection cells ahead of the solidifying front as well as convection cells to the sides of the highly curved mushy-all-liquid solidification interface.

The results from the simulation with the straight-sided alumina mold with the same thermal history, but solidified under normal gravitational condition show showed significant radial macrosegregation and curvature of the solidifying front demonstrating the hallmark steepling that occurs at slow solidification rates. The convection and curvature of the solidifying front can be seen in Figure 7(b).

Figure 7(c) shows the horizontal component of the heat flux for a steepling simulation. Only the horizontal component is shown; the vertical component is much greater. There is a horizontal heat flux because the mold material is an additional pathway for heat flow [58-[59]60]. The heat fluxes in the mold and liquid regions far away from the solidification front are mostly parallel to gravity with little horizontal component. The solidification front distorts the temperature field since the forming solid has roughly twice the thermal diffusivity of the liquid it replaced. This gives less resistance to the flow of heat and depresses the temperature in the alloy, causing a radial flow of heat from the mold into the melt ahead of the solidification front. In turn, the heating on the edges leads to the central dendrites being slightly cooler and farther ahead of the dendrites near the sides of the mold.

A horizontal density gradient develops since there is solute-enriched liquid ahead of the central dendrites, and this liquid is denser than the bulk liquid. Any horizontal density gradient is unstable in a gravitational field, so convection starts towards the sides of the crucible sweeping the enriched solute with it and leading to significant macrosegregation towards the outer edges of the alloy. The convection cells on the sides of the front do not rise far above the solidifying front. The liquid in these cells is enriched in solute and is denser than the bulk liquid of the initial concentration ahead of the solidification front. Thus, the enriched liquid can only rise to the level of the bulk liquid before it loses buoyancy and cycles again.

Most alloys have solid phases with higher thermal diffusivities than their liquid phases, and because of this, dendrite clustering is usually towards the central region of the solidifying alloy. If the thermal diffusivity of the liquid were greater than that of the solid, the opposite would be seen with a central region of macrosegregation with dendrite clustering to the outside. The relative thermal conductivity of the mold material to the alloy can also play a role in clustering to the inside or outside. Steepling is sensitive to the temperature profile applied at the outside of the mold and asymmetries in temperature profile are likely the cause of steepling to a particular side.

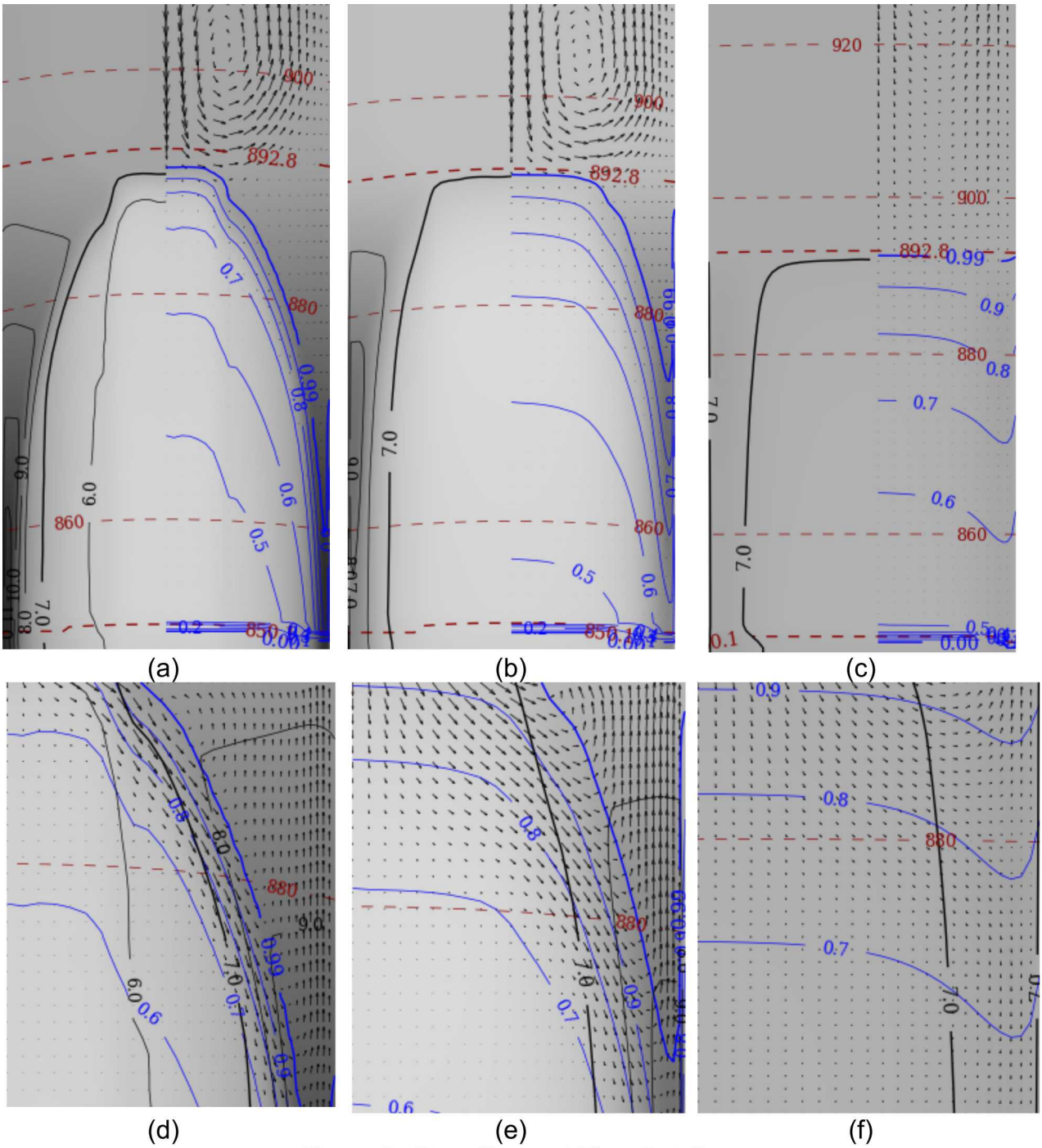

Figure 8. Steepling and Flow Details.

Simulations results: gray-scale shows Si concentration with darker showing higher concentration. Dashed lines are isotherms. (a-c) shows the steepled mushy-zone for solidification rates of 10, 29.1, and 72 μm/s respectively. Left side of each subfigure shows isoconcentrates, the right side shows isopleths of fraction liquid and the vectors show flow of the liquid. (d-f) show detailed views of steepling flow at the edges of the mushy zone for solidification rates of 10, 29.1, and 72 μm/s, respectively. Isopleths and isoconcentrates are both shown here.

The first thing of note in the simulations of the actual terrestrial experiments, shown in Figure 8(a) and Figure 8(b), is the rounded interface that is the characteristic of steepling mushy zones. The shape is closely reminiscent of the quenched longitudinal microstructures obtain by experimentalists [16,19]. The solidification rate increases from left to right, showing how this changes the shape from bullet-like with eutectic or near-eutectic composition liquid on the edges at slow speeds to plug-like shape at higher rates with little variation in the overall composition. This matches previous experimental observations [16].

As can be seen in Figure 8(a), there is strong convection ahead of the mushy zone relative to the convection within it; the difference in flow speeds is roughly twenty-fold. The convection ahead of the mushy zone is thermally driven rather than by differences in solute concentration. The heating on the edges is caused partly by the heat supplied by the furnace to the alloy above the adiabatic zone. The Bridgman furnace used had an adiabatic zone, which is intended to reduce the radial temperature gradient from the heating elements. Even a furnace with a perfectly insulating adiabatic zone would show similar convection because of heat flow through the crucible. As stated previously, when the alloy solidifies, its thermal diffusivity roughly doubles, and this change in thermal diffusivity makes it easier for heat to flow through the alloy leading to a radial heat flux inwards. These two inward-radial heat fluxes are responsible for the strong thermal convection ahead of the mushy zone. The central dendrites are cooler than the edges, and the convection starts the steepling by advecting solute away from the central dendrite tips to the edges. It is interesting to note that the more steepled the interface, the stronger is the thermal convection ahead of it, in these particular cases.

Figure 8(d-f) are side-detail views showing thermal-solutal convection causing the classical cascade of cold, solute-rich liquid from the central dendrites to the outer region. At the casting-mold interface, the inward-radial heat flux increases the buoyancy of the liquid causing an upward flow. The overall effect is a rapid accumulation of solute towards the outer edges of the alloy, which further inhibits solidification. Again, since the solid has twice the thermal diffusivity of the liquid, this further exacerbates the radial temperature gradient and thereby increases the strength of the convection.

There is some difficulty in comparing two-dimensional simulations to three-dimensional experiments because of the coordinate system mismatch. The simulations were done in two-dimensional Cartesian coordinates while an axisymmetric coordinate system, at minimum, would be needed to describe the experiments. It was found that if the quantitative comparisons were made on an area fraction basis, then reasonable comparison could be made between the simulations and the experiments. For two-dimensional Cartesian coordinates, the area fraction is simply

$$f = \frac{x}{W/2} \qquad (34)$$

where x is measured from the center of the simulation domain and W is the width of the sample and is taken as $W = 2R$, where R is the radius of the experimental sample. For the cylindrical samples

$$\boldsymbol{f = \frac{r^2}{R^2}} \quad (35)$$

where r was measured from the center of the steepled portion of the sample. The basic rationalization for this system is that in the two-dimensional simulations, solute is advected from the inner to outer regions on a per-length basis, while in the experiments it is advected from the central region, to the outer edges on a per-area basis. This system ignores subtleties of the fluid flow and solute transport in the real samples, but it allows the comparisons between the two dimensional simulations and the physical experiments. The comparisons are presented in Figure 9.

Schneider and Beckerman [61] give a formulation for a global macrosegregation index.

$$\boldsymbol{S_{rms} = \left(\frac{1}{\mathrm{V}} \int_V \left(\frac{\bar{C}}{C_{ref}} - 1 \right)^2 dV \right)^{\frac{1}{2}}} \quad (36)$$

This is an overall measurement of the degree of macrosegregation in a sample and can be computed for both the experimental results and simulations. The minimum of the macrosegregation index is zero (no macrosegregation) and the theoretical maximum is dependent on the alloy system, but a Scheil segregation profile gives a maximum upper bound of 0.76 for Al-19wt%Cu and 0.81 for Al-7wt%Si. In the experimental measurements, the integration was carried out over the area of the transverse section, while in the simulations it was a line integral across the location of the transverse section rather than a volume integral over the whole domain. The results are presented in Table 3.

The Rayleigh number is a measure of the tendency of a system to undergo natural convection, in this case the tendency for steepling to occur. Note the much higher number for Al-Cu alloys, this should be consistent across forms of the Rayleigh number because the solutal expansion coefficient is more that an order of magnitude larger than in Al-Si alloys and most of the rest of the parameters will be comparable between alloys.

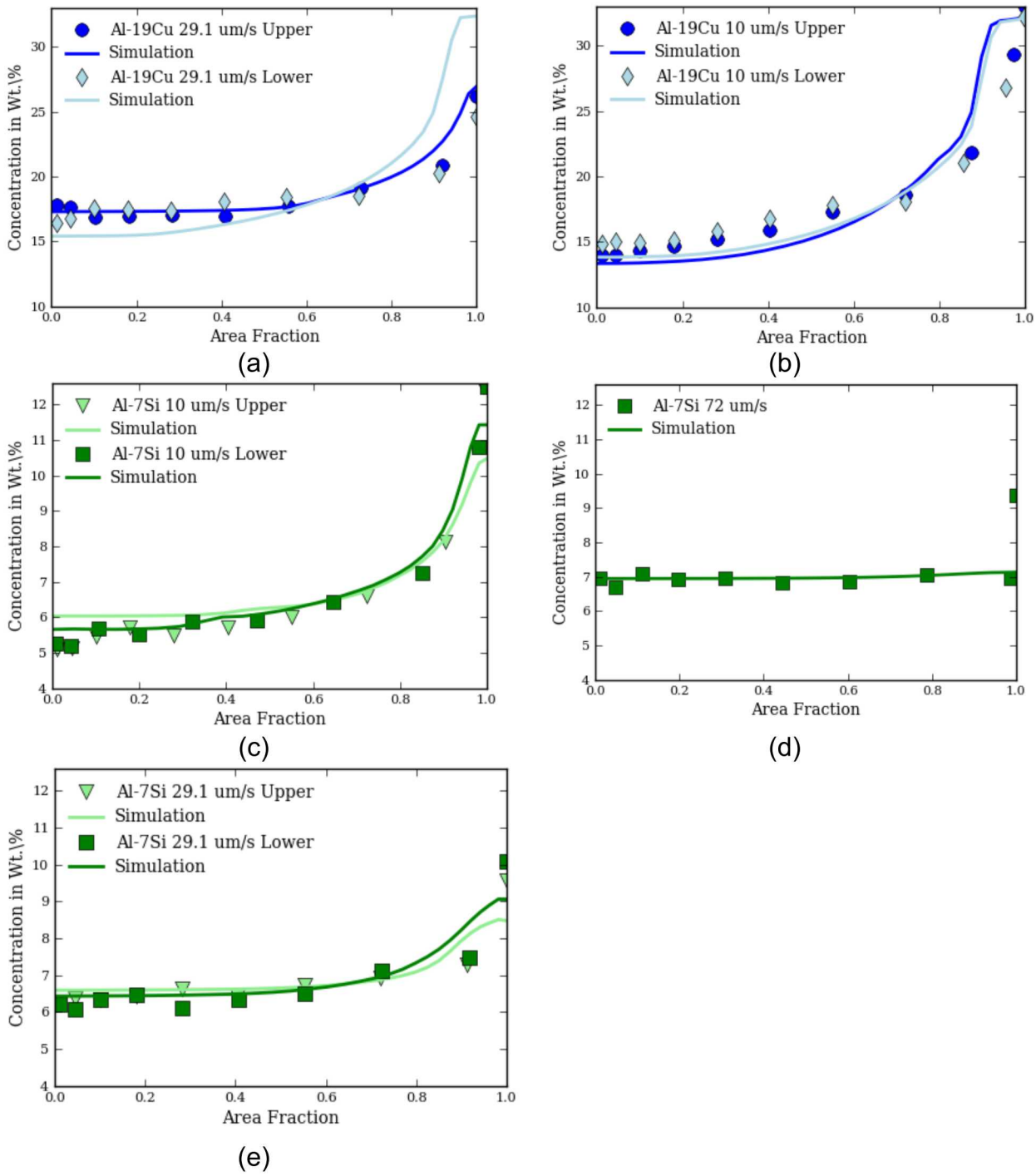

Figure 9. Simulations Compared with Experimental Results.
Comparison on an area fraction basis for all five experiments and nine measurements. Lines are simulations, and points are experimentally measured data from Johnson et al. [46] Data from Johnson et al. [46] have been normalized to the nominal composition of the alloy. (a) Al-19wt%Cu alloy solidified at 10 µm/s (b) Al-19wt%Cu alloy solidified at 29.1 µm/s; (c) Al-7wt%Si alloy solidified at 10 µm/s; (d) Al-7wt%Si alloy solidified at 29.1 µm/s; (e) Al-7wt%Si alloy solidified at 72 µm/s.

Table 3. Simulation Results Summary

Sample	Gradient (K/m)	Rate μm/s	d_A, μm	Exp. S_{rms}	Sim. S_{rms}
Al-7%Si Lower	3300	10	789	0.205	0.202
Al-7%Si Upper	4000	10	508	0.218	0.155
Al-7%Si Lower	5100	29.1	506	0.112	0.105
Al-7%Si Upper	5100	29.1	461	0.087	0.077
Al-7%Si	4900	72	398	0.025	0.008
Al-19%Cu Lower	8100	10	361	0.191	0.284
Al-19%Cu Upper	9200	10	420	0.218	0.305
Al-19%Cu Lower	4800	29.1	486	0.082	0.236
Al-19%Cu Upper	5300	29.1	303	0.106	0.118

4.5 Discussion

The simulations of the Al-19wt%Cu system fit reasonably to the experimental data in three of four cases. There are a few suspected reasons for the poor correlation in case of the lower sample of Al-19wt%Cu grown at 29.1 μm/s, where the simulation does not match the experimental results. The simulation predicts strong thermal convection ahead of the mushy zone in the location of this transverse section. This leads to the development of a strongly steepled interface. In the experiment, this steepled interface did not develop as strongly. The eutectic constituent is present mainly in one quadrant of the transverse section. This segregation could not have developed because of an axisymmetric flow, so the flow could not be well approximated in a two-dimensional simulation. This may have been caused by a non-uniform radial heating, but it would take multiple thermocouples around the circumference of the sample to detect this.

It was also noticed that, in this particular transverse section, there were several grains, while most of the other sections had one or few. It is theorized that grains with different crystal orientations could affect steepling flow, and this could lead to non-radial steepling. The permeability model used in the simulations assumes a parallel alignment of the trunks of the dendrites with the direction of growth, and it can be seen that several of the grains are not parallel. Nucleating grains would also interrupt steepling. In the same sample, past the constriction in cross section, the transverse section only had two or three grains that were well aligned with the direction of growth, and the agreement between the simulation and experiment is quite good.

In the simulations of Al-19wt%Cu grown at 10 μm/s, the outer edges were of eutectic composition. In the experiments, there was always one edge that was entirely of the eutectic micro-constituent, as can be seen in Figure 6. These experiments showed the largest regions of eutectic constituent as predicted by the simulations; however, they were never very radially distributed, so the match with the simulation is not as good as with the Al-7wt%Si. Al-7wt%Si alloy samples tended to have very regular radial

distributions, which can be seen in Figure 6(a), whereas the steepling in the Al-19wt%Cu alloy is more distorted, as seen in Figure 6(b). It is hypothesized that, since the Al-Cu alloys have a much denser solute and are more prone to steepling, the non-radial steepling is more likely to persist during solidification since steepling tends to be self-reinforcing. In the Al-Si alloys, it appears that the steepling is more controlled and organized by the thermal convection ahead of the mushy zone.

The simulated results for Al-7wt%Si alloys agree well with the experimentally measured macrosegregation. The upper transverse section of the Al-7wt%Si sample solidified at 10 μm/ showed slightly more sever steepling than predicted by the simulations. In the simulation shown in Figure 8, it is thought that the wiggle in the isopleth of fraction liquid delimiting the beginning of the mushy zone is because of the stronger thermal convection ahead of it. In simulations with strong thermal convection ahead of the mushy zone, the bullet shape of the leading front of the mushy zone is more interrupted than those with weak convection. It is interesting to note that even though in the simulation there is some radial flow in the sample that was solidified at 72 μm/s, there is almost no measureable macrosegregation, indicating that steepling is a strong function of solidification rate.

5. DIRECTIONAL SOLIDIFICATION IN SHAPED CASTINGS

For investigating solidification through changes in cross section, the same solidification model from the previous section was used. The same thermal data and extrapolation methods were used from the previous section and all boundary conditions where the same as previously stated. The mesh was modified slightly to have a higher resolution in the regions of the changes in cross section since that was the area of particular interest for this investigation. Heat flow through the mold has a large effect on solidification in these regions, so simulations with hypothetical molds made from alumina were also run to contrast with the actual experiments which were performed with graphite molds. Unfortunately similar experiments in alumina molds have not yet been run for verification of the results. All material data used was the same as the previous section and is given in Table 2. Longitudinal micrographs and analysis of the regions of change in cross section have only been completed for the Al-7wt%Si experiments solidified at 10 μm/s, so these will be the only experiments discussed here. The results of the Al-19wt%Cu simulations are qualitatively similar in what occurred, but since data from actual experiments is lacking, they will be omitted.

5.1 Results

The simulations of solidification in molds with changing cross sections showed a significant difference in convection and macrosegregation profile between the two mold materials in the contracting region. However there was much less difference in the expanding region, but still a few slight ones. The results from both changes in cross section and both mold materials are shown and discussed, and the final macrosegregation profiles are compared with those obtained from the experiment.

5.1.1 Solidifying Into a Contraction

When the solidification front is a few centimeters below the change in cross section it is curved and steepled, as we have seen in the previous section, in both types of molds. The steepling is caused by a depression in the temperature of the alloy from both the contraction in cross section of the mold and the lower thermal diffusivity of the mold material relative to that of the liquid alloy. Not enough heat is flowing into the alloy to maintain a steep gradient past the contraction, so heat flows in from the sides. In this region the heating from the sides is much more pronounced than in the regions of the casting with a uniform cross section.

The two molds have markedly different flow patterns in the vicinity of the contraction in cross section when the solidification front is still a few centimeters away. Figure 11(a) shows the graphite mold with heat flowing from the mold to the alloy because of the higher thermal conductivity of the liquid alloy. This heating creates long convection cells along the walls that travel from the solidifying region to the change in cross section. In the alumina mold simulation, shown in Figure 10(b), these convection cells are also present on the sides of the liquid alloy, but do not extend completely to the contraction.

The thermal diffusivity of alumina is an order of magnitude lower than that of the alloy, so at the contraction there is a significant distortion of the temperature field. With the more thermally conductive melt above it, the liquid in the neck region is hotter than the outside and begins to rise due to thermal buoyancy. This creates counter-rotating convection cells below the contraction, which has very different results when the solidification front reaches the change in cross section.

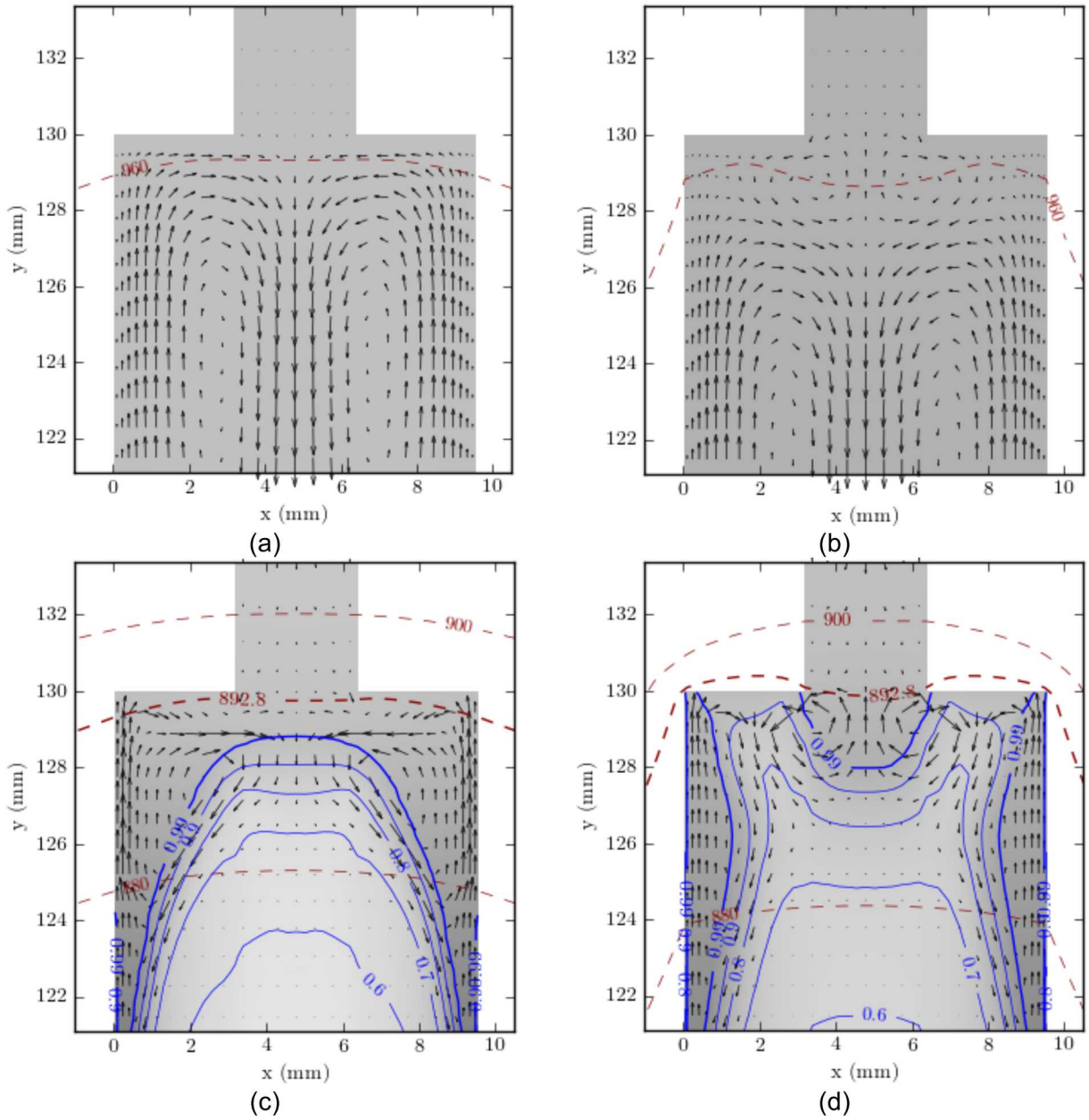

Figure 10. Solidifying into a Contraction.
Al-7wt%si alloy solidifying into a contraction. (a) fluid flow in the graphite mold. (b) fluid flow in the alumina mold. (c) the solidification front in the graphite mold. (d) the solidification front in the alumina mold.

In the graphite mold, Figure 10(c), when the front reaches the contraction, it remains steepled moving into the neck. This results in significant macrosegregation outwards to the sides and onto the shelf of the change in cross section. In the alumina mold, Figure 10d, when the solidification front reaches the counter-rotating cell in the neck, the shape of the mushy-liquid interface is changed by the temperature field and advection of solute to the center of the sample, which inhibits solidification there. The cold liquid near the shelves of the contraction still has the nominal solute concentration and solidifies rapidly even as the solute-enriched liquid on the outside has not yet started to solidify.

5.1.2 Solidifying Out of an Expansion

Comparing Figure 11(a) of the graphite mold and Figure 11(b) of the alumina, the convection in the expansion area is localized in the lower thermal diffusivity alumina mold, when compared to the graphite mold, but in the same direction. In the alumina mold, the distortion of the temperature field is much greater at the expansion in cross section as evidenced by the bending isotherm. However, this convection also dies off far more quickly than in the graphite mold which has convection driven from a slight heating at the vertical alloy-mold interface, while the expansion in the alumina mold blocks heat flow from the alloy and redirects it outward into the mold.

As the solidification front enters the expansion it looks rather similar in both types of molds, but the flow in the all-liquid region is different between them. In the graphite mold, Figure 11(c), there is still an inward heat flux from the edge of the mold that is responsible for the strong convection cells present. In the alumina mold, Figure 11(d), the heat flux through the alloy is resisted by the change in cross section, and temperature is elevated in the alloy. Some of the heat flux then flows from the alloy into the mold and meaning there is cooler liquid at the edges causing convections cells in the reverse direction from the graphite mold.

At the leading part of the mushy zone, the convection is driven by solutal buoyancy differences as the interdendritic liquid, more enriched with solute, flows to the lower, outer edges of the mold ahead of the solidification front. This solute-enriched liquid inhibits solidification at the outer edges and is why the mushy-liquid interface does not conform to the nominal liquidus isotherm in either case.

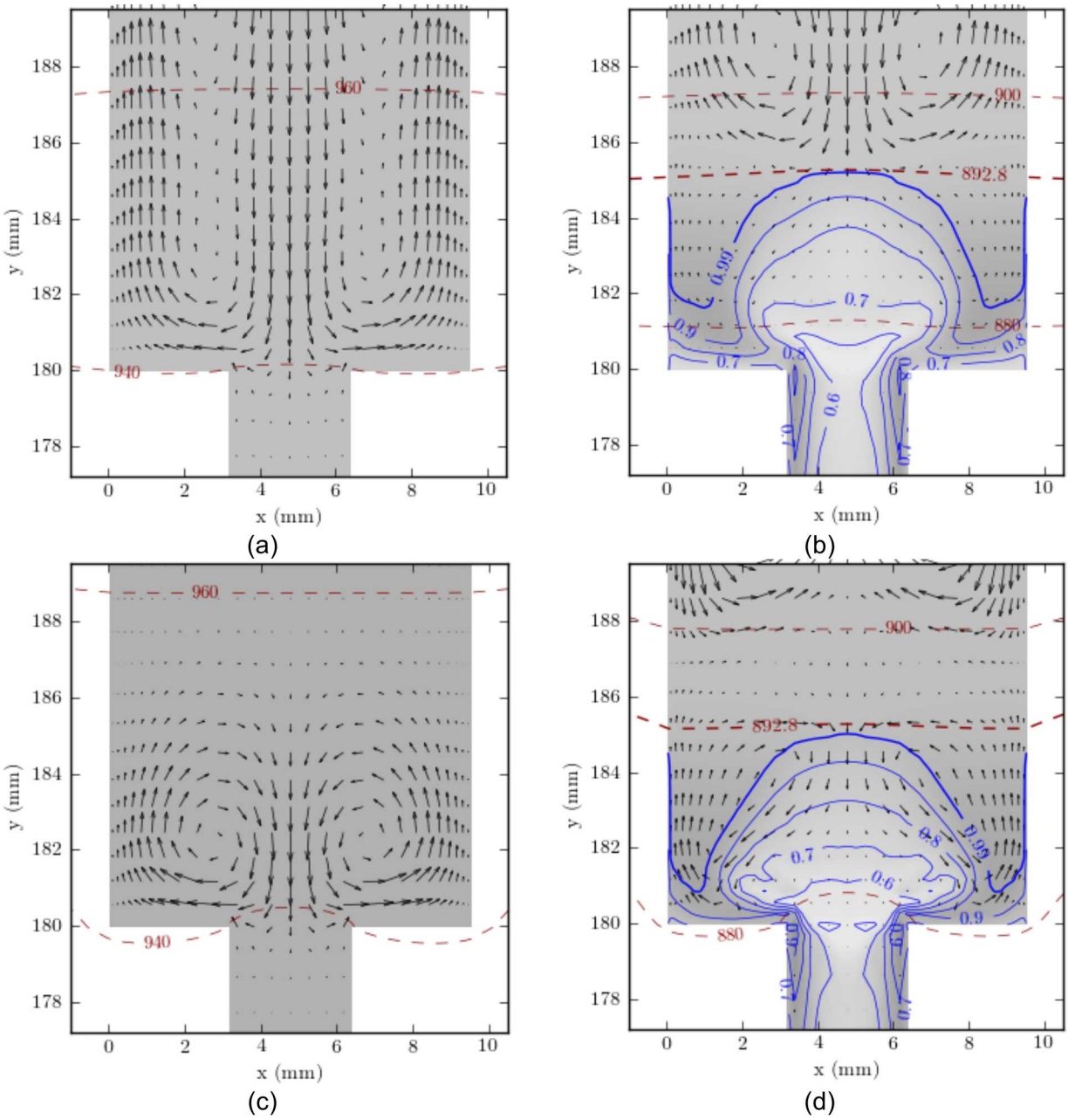

Figure 11. Solidifying Out of an Expansion.
Al-7wt%si alloy solidifying out of an expansion. (a) fluid flow in the graphite mold. (b) fluid flow in the alumina mold. (c) the solidification front in the graphite mold. (d) the solidification front in the alumina mold.

5.2 Comparison of Final Macrosegregation Profiles

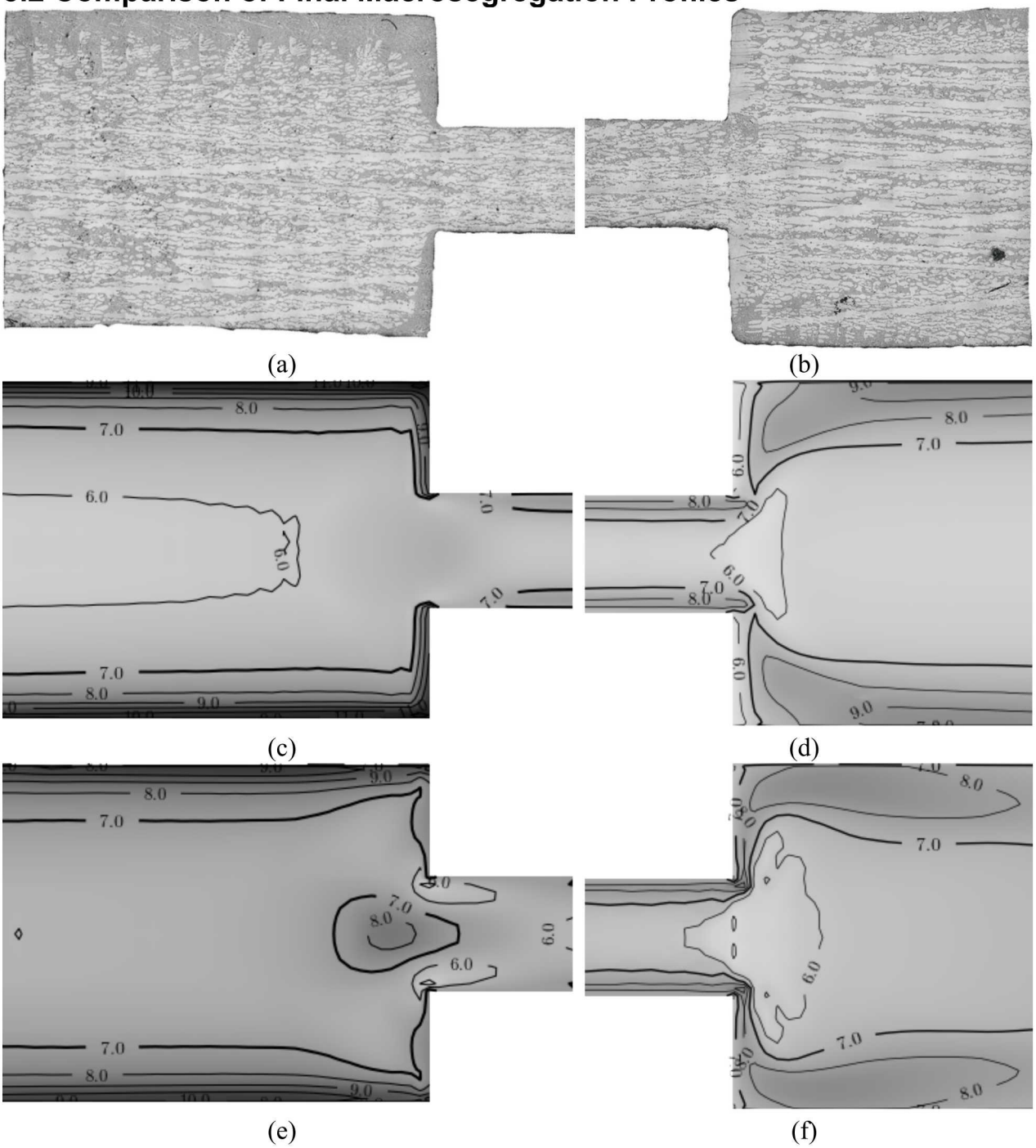

Figure 12. Final Concentration Profiles.
Macrostructures from the experiment and solute concentration plots from the simulations. Solidification was vertical, from left side to right. (a) contraction region. (b) expansion region. (c)-(d) same regions from the graphite mold simulation. (e)-(f) same regions from the alumina mold simulation. All contours are in wt.%.

Macrostructures of the experimental sample are shown in Figure 12(a) and Figure 12(b). The macrosegregation in Figure 12(a) is evident on the top edge of the stitched micrographs and at the shelves of the constriction. The macrosegregation at the top edge is the result of steepling. It is thought that some asymmetry in the processing of the sample is responsible for the steepling to only one side. From transverse micrographs of the sample, asymmetric steepling is present both above and below the constriction. Possible causes would be a slight misalignment with gravity or a slightly asymmetric temperature profile during solidification since convection is very sensitive to either of these. It is also possible that the convection pattern is unstable to any perturbation, but this needs further study. These experiments and phenomena are inherently three dimensional, while the simulations are two dimensional. Fluid flow in two dimensions is simplified compared with three dimensions, and many flows cannot be adequately captured.

The calculated macrosegregation profiles for solidification in both types of molds are shown in Figure 12(c-f). Comparing the concentration profile of the simulated graphite mold, Figure 12(c) with the macrostructure of the contraction, it can be seen that the major macrosegregation features were captured. In the simulation, symmetric temperature boundary conditions were applied and gravity was perfectly vertical, so the asymmetry seen in Figure 12(a) is not present. The steepling caused macrosegregation to the outer edges is present, and near eutectic compositions are expected on the outer edge, which is what is seen in the experiment. When the solidification front was interrupted by the constriction, macrosegregation occurred because of the impinged solute boundary layer ahead of the solidification front and diffusion of solute down the concentration gradient in the mushy zone to the shelf. This is seen in both the simulation and the experimental micrograph.

At the expansion, shown in Figure 12(d), less macrosegregation is predicted and less macrosegregation can be seen. Some negative macrosegregation (regions of solute depletion) can be seen just off the shelves of the expansion in cross section. This occurred because of diffusion of solute down the concentration gradient in the mushy zone. Since no solute can diffuse from the mold, a depleted region develops. The visual amount of eutectic increases slightly at the outer edges of the sample and the simulation predicts an increase in solute concentration towards the edges as well. Past the region shown, the simulation shows slight steepling and macrosegregation towards the edges, and this can also be seen in the upper right quadrant of the micrograph shown in Figure 13. The asymmetry in steepling is again present.

Comparing the simulations of the different mold materials, the most striking difference is the region of positive macrosegregation in the neck of the alumina mold, shown in Figure 12(e). This positive macrosegregation was formed by the distortion in the temperature field and the subsequent thermosolutal convection that advected solute to the center of the neck, seen in Figure 10(d). The segregation at the shelf of the cross-section change of the alumina mold simulation was not as pronounced since it solidified more quickly because of the flow pattern and lower temperatures; this can be seen by comparing Figure 10(d) and Figure 10(c)

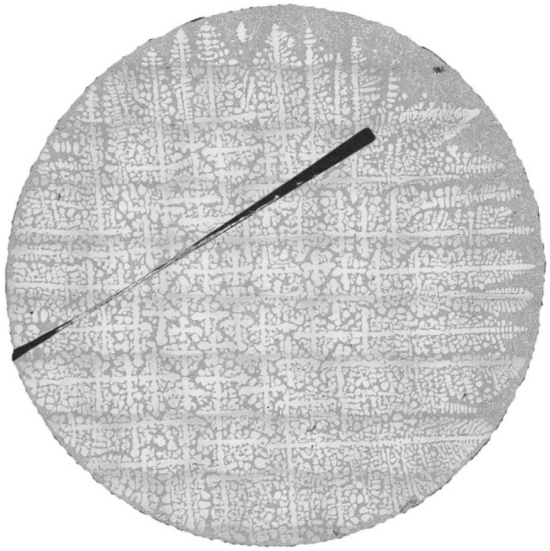

Figure 13. Transverse Micrograph from Al-7wt%Si Sample
Transverse micrograph from past the expansion in cross section at y ≈ 190mm.

The two mold materials produce rather similar results at the expansion in cross section, which are shown in Figure 12(d) and Figure 12(e). This is not surprising given the convection in the region was similar in direction for both simulations. The only noteworthy difference is that in the graphite mold there is some outward segregation, characteristic of steepling, as the front moved beyond the change in cross section while the macrosegregation in the alumina mold died out more quickly. In the alumina mold, Figure 12(e), the negative macrosegregation on the shelf is less, and the center region of negative macrosegregation is slightly larger because of the greater distortion in the temperature field as can be seen by the bending isotherms Figure 11(b). Overall, both molds show less macrosegregation in the expansions than in the contractions, which probably relates to the impinging boundary layer of solute ahead of a solidification front.

6. CONCLUSIONS

The first, melting, model presented can capture the macrosegregation caused by thermal gradient zone melting in the mushy zone of an Al-7 wt.% Si alloy. The model, which tracks fraction liquid and overall concentration, is consistent with, but more general than the equation given by Pfann [38], which predicts the migration of droplets in the mushy zone. The model has inherent instabilities caused by the discontinuities that develop in the fraction liquid at the dendrite tips as they melt backwards. These instabilities can be made stable by using an upwinding scheme. The model somewhat underpredicts the macrosegregation, particularly in the region of the dendrite tips. There are uncertainties in the diffusion coefficient and application of the model, but in its present form, the model captures the major redistribution of solute during temperature gradient zone melting.

The second, solidification, model can make a good estimate of the degree of macrosegregation in steepled castings. If the macrosegregation is well describe on a radial basis, then macrosegregation can be captured by a two-dimensional simulation when compared on an area fraction basis. In the Al-7wt%Si alloy, a high degree of quantitative agreement can be achieved between the simulations and experimental results when compared on an area fraction basis. Three-dimensional simulations are probably required to capture asymmetries in processing and to make complete quantitative macrosegregation comparisons. Al-Cu alloys probably require three-dimensional simulations and very thorough instrumentation of the experiments to fully understand their steepling behavior. Otherwise an alloy with a lower copper concentration, processed under conditions less prone to steepling, may allow better comparisons with two-dimensional simulations.

In shaped, directionally-solidified castings, the mold materials and changes in cross section together create conditions for macrosegregation. In this particular set of experiments and simulations of solidification in a graphite mold, the solidification into a contraction caused more marked-macrosegregation features that could be well predicted using the model. The model also predicted that a mold with a lower thermal diffusivity would result in a different macrosegregation pattern. In solidification out of an expansion, there were fewer macrosegregation features observed or predicted by the model. Since the two molds simulated resulted in similar convection patterns in the expansion, similar macrosegregation patterns were observed.

This study showed that the mold should be included in numerical simulations of directional solidification because of its effect on the temperature field. It also presents the possibility of engineering the mold to avoid or mitigate the effects of thermosolutal convection and macrosegregation by mold-material and geometry choices.

7. REFERENCES

[1] P. Peng, X. Li, Y. Su, D. Liu, J. Guo and H. Fu, "Effect of Peritectic Reaction on the Migration of Secondary Dendrite Arms in the Presence of Tertiary Dendrites: Analysis of a Directionally Solidified Sn 36 At.%Ni Peritectic Alloy," *Journal of Materials Science,* vol. 48, no. 6, pp. 2608-2617, Mar 2013.

[2] S. Fischer, M. Zaloznik, J.-M. Seiler, M. Rettenmayr and H. Combeau, "Experimental Verification of a Model on Melting and Resolidification in a Temperature Gradient," *Journal of Alloys and Compounds,* vol. 540, pp. 85-88, Nov 2012.

[3] D. Liu, X. Li, Y. Su, L. Luo, B. Zhang, R. Chen, J. Guo and H. Fu, "An Analysis of Non-Equilibrium Peritectic Reaction Driven by Solute Diffusion Under a Temperature Gradient," *Journal of Crystal Growth,* vol. 334, no. 1, pp. 195-199, Nov 2011.

[4] D. Liu, X. Li, Y. Su, P. Peng, L. Luo, J. Guo and H. Fu, "Secondary Dendrite Arm Migration Caused by Temperature Gradient Zone Melting During Peritectic Solidification," *Acta Materialia,* vol. 60, no. 67, pp. 2679-2688, Apr 2012.

[5] D. Liu, Y. Su, X. Li, L. Luo, J. Guo and H. Fu, "Influence of Thermal Stabilization on the Solute Concentration of the Melt in Directional Solidification," *Journal of Crystal Growth,* vol. 312, no. 24, pp. 3658-3664, Dec 2010.

[6] Y. Su, D. Liu, X. Li, L. Luo, J. Guo and H. Fu, "Preparation of the Initial Solid-Liquid Interface and Melt in Directional Solidification of Al-18 At%Ni Peritectic Alloy," *Journal of Crystal Growth,* vol. 312, no. 16-17, pp. 2441-2448, Aug 2010.

[7] H. Nguyen Thi, G. Reinhart, A. Buffet, T. Schenk, N. Mangelinck-Noel, H. Jung, N. Bergeon, B. Billia, J. Hartwig and J. Baruchel, "In Situ and Real-Time Analysis of TGZM Phenomena by Synchrotron X-Ray Radiography," *Journal of Crystal Growth,* vol. 310, no. 11, pp. 2906-2914, May 2008.

[8] H. Nguyen Thi, B. Drevet, J. M. Debierre, D. Camel, Y. Dabo and B. Billia, "Preparation of the Initial Solid-Liquid Interface and Melt in Directional Solidification," *Journal of Crystal Growth,* vol. 253, no. 1-4, pp. 539-548, Jun 2003.

[9] U. Bosenberg, M. Buchmann and M. Rettenmayr, "Initial Transients During Solid/Liquid Phase Transformations in a Temperature Gradient," *Journal of Crystal Growth,* vol. 304, no. 1, pp. 281-286, Jun 2007.

[10] B. Li, H. D. Brody and A. Kazimirov, "Synchrotron Microradiography of Temperature Gradient Zone Melting in Directional Solidification," *Metallurgical and Materials Transactions A,* vol. 37, no. 3, pp. 1039-1044, Mar 2006.

[11] D. Benielli, N. Bergeon, H. Jamgotchian, B. Billia and P. Voge, "Free Growth and Instability Morphologies in Directional Melting of Alloys," *Physical Review E,* vol. 65, no. 5, p. 051604, May 2002.

[12] W. G. Pfann, *Temperature Gradient Zone-Melting,* Google Patents, 1957.

[13] N. R. Gewecke and T. P. Schulze, "Solid-Mush Interface Conditions for Mushy Layers," *Journal of Fluid Mechanics,* vol. 689, pp. 357-375, 2011.

[14] N. R. Gewecke and T. P. Schulze, "The Rapid Advance and Slow Retreat of a Mushy Zone," *Journal of Fluid Mechanics,* vol. 674, pp. 227-243, 2011.

[15] G. Salloum Abou Jaoude, G. Reinhart, H. Nguyen-Thi, H. Combeau, M. Zaloznik, T.

Schenk and T. Lafford, "In Situ Experimental Observation of the Time Evolution of a Dendritic Mushy Zone in a Fixed Temperature Gradient," *Comptes Rendus Mecanique,* vol. 341, no. 4-5, pp. 421-428, Apr 2013.

[16] M. H. Burden, D. J. Hebditch and J. D. Hunt, "Macroscopic Stability of a Planar, Cellular or Dendritic Interface during Directional Freezing," *J. Cryst. Growth,* vol. 20, no. 2, pp. 121-124, 1973.

[17] D. G. McCartney and J. D. Hunt, "Measurements of Cell and Primary Dendrite Arm Spacings in Directionally Solidified Aluminium Alloys," *Acta Metall.,* vol. 29, no. 11, pp. 1851-1863, 1981.

[18] J. T. Mason, J. D. Verhoeven and R. Trivedi, "Primary Dendrite Spacing: Part II. Experimental Studies of Pb-Pd and Pb-Au alloys," *Metall. Mater. Trans. A,* vol. 15A, no. 9, pp. 1665-1676, 1984.

[19] J. D. Verhoeven, J. T. Mason and R. Trivedi, "The Effect of Convection on the Dendrite to Eutectic Transition," *Metall. Mater. Trans. A,* vol. 17A, no. 6, pp. 991-1000, 1986.

[20] H. Nguyen Thi, Y. Dabo, B. Drevet, M. D. Dupouy, D. Camel, B. Billia, J. D. Hunt and A. Chilton, "Directional Solidification of Al-1.5wt%Ni Alloys under Diffusion Transport in Space and Fluid-Flow Localisation on Earth," *J. Cryst. Growth,* vol. 281, no. 2-4, pp. 654-668, 2005.

[21] B. Billia, H. N. Thi, G. Reinhart, Y. Dabo, B. H. Zhou, Q. S. Liu, T. Lyubimova, B. Roux and C. W. Lan, "Tailoring of Dendritic Microstructure in Solidification Processing by Crucible Vibration/Rotation," *Microgravity - Sci. Tech.,* vol. 16, no. 1-4, pp. 15-19, 2005.

[22] C. Weiss, N. Bergeon, N. Mangelinck-Noel and B. Billia, "Effects of the Interface Curvature on Cellular and Dendritic Microstructures," *Mater. Sci. Eng.: A,* Vols. 413-414, pp. 296-301, 2005.

[23] B. H. Zhou, H. Jung, N. Mangelinck-Noel, H. Nguyen-Thi, B. Billia, Q. S. Liu and C. W. Lan, "Comparative Study of the Influence of Natural Convection on Directional Solidification of Al-3.5wt%Ni and Al-7wt%Si Alloys," *Adv. Space Res.,* vol. 41, no. 12, pp. 2112-2117, 2008.

[24] G. Reinhart, C.-A. Gandin, N. Mangelinck-Noel, H. Nguyen-Thi, B. Billia and J. Baruchel, "Direct Simulation of a Directional Solidification Experiment Observed in Situ and Real-Time Using X-Ray Imaging," *IOP Conf. Ser.: Mater. Sci. Eng.,* vol. 33, no. 1, p. 012077, 2012.

[25] S. D. Felicelli, D. R. Poirier and J. C. Heinrich, "Macrosegregation Patterns in Multicomponent Ni-Base Alloys," *J. Cryst. Growth,* vol. 177, no. 1-2, pp. 145-161, 1997.

[26] S. D. Felicelli, D. R. Poirier, A. F. Giamei and J. C. Heinrich, "Simulating Convection and Macrosegregation in Superalloys," *JOM,* vol. 49, no. 3, pp. 21-25, 1997.

[27] S. D. Felicelli, J. C. Heinrich and D. R. Poirier, "Finite Element Analysis of Directional Solidification of Multicomponent Alloys," *International Journal for Numerical Methods in Fluids,* vol. 27, no. 1-4, pp. 207-227, 1998.

[28] D. Xu, "A Unified Microscale Parameter Approach to Solidification-Transport Process-Based Macrosegregation Modeling for Dendritic Solidification: Part II. Numerical Example Computations," *Metall. Mater. Trans. B,* vol. 33B, no. 3, pp. 451-463, 2002.

[29] D. Xu, J. Guo, H. Fu and W. Bi, "Influences of Dendrite Morphologies and Solid-Back

Diffusion on Macrosegregation in Directionally Solidified Blade-Like Casting," *Mater. Sci. Eng.: A,* vol. 344, no. 1-2, pp. 64-73, 2003.

[30] D. Xu, Y. Bai, H. Fu and J. Guo, "Heat, Mass and Momentum Transport Behaviors in Directionally Solidifying Blade-Like Castings in Different Electromagnetic Fields Described Using a Continuum Model," *International Journal of Heat and Mass Transfer,* vol. 48, no. 11, pp. 2219-2232, 2005.

[31] Y. Bai, D. Xu, L. Mao, J. Guo and H. Fu, "FEM/FDM-Joint Simulation for Transport Phenomena in Directionally Solidifying Shaped TiAl Casting under Electromagnetic Field," *ISIJ International,* vol. 44, no. 7, pp. 1173-1179, 2004.

[32] A. J. Elliott, T. M. Pollock, S. Tin, W. T. King, S.-C. Huang and M. Gigliotti, "Directional Solidification of Large Superalloy Castings with Radiation and Liquid-Metal Cooling: a Comparative Assessment," *Metall. Mater. Trans. A,* vol. 35, no. 10, pp. 3221-3231, 2004.

[33] A. J. Elliott and T. M. Pollock, "Thermal Analysis of the Bridgman and Liquid-Metal-Cooled Directional Solidification Investment Casting Processes," *Metall. Mater. Trans. A,* vol. 38, no. 4, pp. 871-882, 2007.

[34] R. Sellamuthu, H. D. Brody and A. F. Giamei, "Effect of Fluid Flow and Hafnium Content on Macrosegregation in the Directional Solidification of Nickel Base Superalloys," *Metall. Mater. Trans. B,* vol. 17, no. 2, pp. 347-356, 1986.

[35] M. C. Flemings and G. E. Nereo, "Macrosegregation. Part. 1," *AIME Met Soc Trans,* vol. 239, no. 9, pp. 1449-1461, 1967.

[36] D. R. Poirier, "Density, Viscosity, and Diffusion Coefficients in Hypoeutectic Al-Si Liquid Alloys: An Assessment of Available Data," *Metallurgical and Materials Transactions B,* pp. 1-10, Feb 2014.

[37] S. Fischer and M. Rettenmayr, "Observation of Early Melting Stages of an Al - Cu Alloy in a Temperature Gradient," *International Journal of Materials Research,* vol. 102, no. 10, pp. 1226-1231, Oct 2011.

[38] W. G. Pfann, Zone Melting, New York, NY: Wiley, 1966.

[39] J. E. Guyer, D. Wheeler and J. A. Warren, "FiPy: Partial Differential Equations with Python," *Computing in Science & Engineering,* vol. 11, no. 3, pp. 6-15, May 2009.

[40] S. D. Felicelli, J. C. Heinrich and D. R. Poirier, "Simulation of Freckles during Vertical Solidification of Binary Alloys," *Metall. Mater. Trans. B,* vol. 22B, no. 6, pp. 847-859, 1991.

[41] S. D. Felicelli, J. C. Heinrich and D. R. Poirier, "Numerical Model for Dendritic Solidification of Binary Alloys," *Numer. Heat Transfer, Part B,* vol. 23, no. 4, pp. 461-481, 1993.

[42] D. R. Poirier, P. J. Nandapurkar and S. Ganesan, "The Energy and Solute Conservation Equations for Dendritic Solidification," *Metall. Mater. Trans. B,* vol. 22B, no. 6, pp. 889-900, 1991.

[43] S. Ganesan and D. R. Poirier, "Conservation of Mass and Momentum for the Flow of Interdendritic Liquid during Solidification," *Metall. Mater. Trans. B,* vol. 21B, no. 1, pp. 173-181, 1990.

[44] E. McBride, J. C. Heinrich and D. R. Poirier, "Numerical Simulation of Incompressible Flow Driven by Density Variations during Phase Change," *Int. J. Numer. Methods Fluids,*

vol. 31, no. 5, pp. 787-800, 1999.

[45] C. Frueh, D. R. Poirier and S. D. Felicelli, "Predicting Freckle-Defects in Directionally Solidified Pb-Sn Alloys," *Mater. Sci. Eng.: A,* vol. 328, no. 1-2, pp. 245-255, 2002.

[46] L. Johnson, M. Ghods, M. A. Lauer, S. N. Tewari, R. N. Grugel and D. R. Poirier, *Radial Macrosegregation and Steepling in Directionally Solidified Al-7Si and Al-19Cu Alloys,* 2014.

[47] C. Frueh, D. R. Poirier and S. D. Felicelli, "Effect of Computational Domain Size on the Mathematical Modeling of Transport Processes and Segregation during Directional Solidification," *Metall. Mater. Trans. A,* vol. 31A, no. 12, pp. 3129-3135, 2000.

[48] S. Ganesan and D. R. Poirier, "Densities of Aluminum-rich Aluminum-Copper Alloys during Solidification," *Metallurgical Transactions A,* vol. 18A, no. 5, pp. 721-723, 1987.

[49] S. Ganesan, R. Speiser and D. R. Poirier, "Viscosities of Aluminum-rich Al-Cu Liquid Alloys," *Metallurgical and Materials Transactions B,* vol. 18B, no. 2, pp. 421-424, 1987.

[50] A. P. Boeira, I. L. Ferreira and A. Garcia, "Alloy Composition and Metal/Mold Heat Transfer Efficiency Affecting Inverse Segregation and Porosity of As-Cast Al-Cu Alloys," *Materials & Design,* vol. 30, no. 6, pp. 2090-2098, 2009.

[51] D. R. Poirier and E. McBride, "Thermal Conductivities of Hypoeutectic Al-Cu Alloys during Solidification and Cooling," *Mater. Sci. Eng.: A,* vol. 224, no. 1-2, pp. 48-52, 1997.

[52] D. R. Poirier, *Transport and Thermodynamic Properties for Solidification of Al-7Si Alloy,* 2011.

[53] R. Taylor, K. E. Gilchrist and L. J. Poston, "Thermal Conductivity of Polycrystalline Graphite," *Carbon,* vol. 6, no. 4, pp. 537-544, 1968.

[54] D. R. Poirier and G. H. Geiger, Transport Phenomena in Materials Processing, Warrendale, PA: TMS, 1998.

[55] W. D. Kingery, Introduction to Ceramics, New York, NY: Wiley, 1960.

[56] A. Butland and R. J. Maddison, "The Specific Heat of Graphite: An Evaluation of Measurements," *Journal of Nuclear Materials,* vol. 49, no. 1, pp. 45-56, 1973.

[57] S. Rattanaweeranon, P. Limsuwan, V. Thongpool, V. Piriyawong and P. Asanithi, "Influence of Bulk Graphite Density on Electrical Conductivity," *Procedia Eng.,* vol. 32, no. 0, pp. 1100-1106, 2012.

[58] B. Billia, N. Bergeon, D. Benielli, Y. Dabo, R. Guerin, H. Jamgotchian, H. N. Thi and P. Voge, "Localized Morphologies Observed in Directional Solidification of Binary Alloys into Three-Dimensional Flows," P. Ehrhard, D. Riley and P. Steen, Eds., Springer Netherlands, 2001, pp. 5-12.

[59] T. Jasinski, A. F. Witt and W. M. Rohsenow, "Heat Transfer Analysis of the Bridgman-Stockbarger Configuration for Crystal Growth: II. Analytical Treatment of Radial Temperature Variations," *J. Cryst. Growth,* vol. 67, no. 2, pp. 173-184, 1984.

[60] C. Barat, T. Duffar and J. P. Garandet, "Estimation of the Curvature of the Solid-Liquid Interface during Bridgman Crystal Growth," *J. Cryst. Growth,* vol. 194, no. 1, pp. 149-155, 1998.

[61] M. C. Schneider and C. Beckermann, "Formation of Macrosegregation by Multicomponent Thermosolutal Convection during the Solidification of Steel," *Metall. Mater. Trans. A,* vol.

26, no. 9, pp. 2373-2388, 1995.

DISTRIBUTION

1 Mark Lauer
The University of Arizona
Department of Materials Science & Engineering
1235 E. James E. Rogers Way
Room 141
P.O. Box 210012
Tucson, AZ 85721–0012

1	MS0351	Duane B. Dimos	Org. 1000
1	MS0885	F. Doug Wall	Org. 1810
1	MS0887	Terry L. Aselage	Org. 1800
1	MS0889	Jonathan D. Madison	Org. 1814
1	MS1411	Amy C. Sun	Org. 1814

1	MS0899	Technical Library	Org. 9536 (electronic copy)
1	MS0359	D. Chavez, LDRD Office	Org. 1911 (electronic copy)


Sandia National Laboratories